A Proximity-Focusing RICH for the ePIC Experiment
– Conceptual Design Report –
(Draft 1.0)

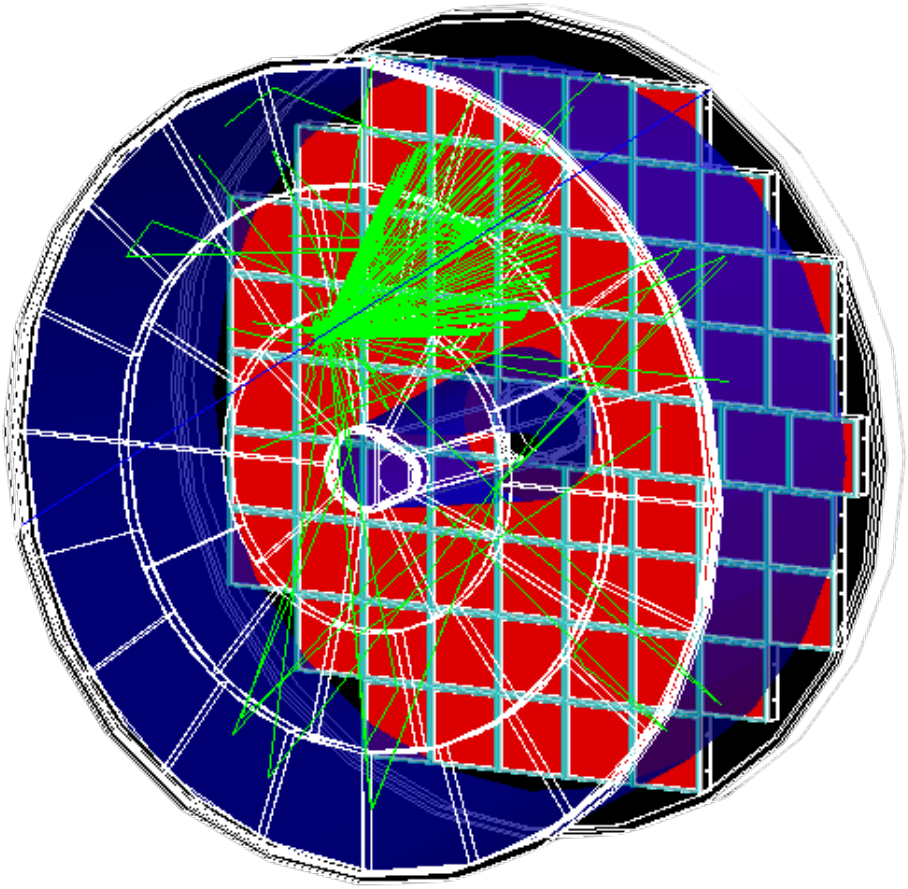

Deb Sankar Bhattacharya[5], Daniel Cacace[4], Helen Caines[11], Chandradoy Chatterjee[5], Jaydeep Datta[1], Abhay Deshpande[1], Christopher Dilks[2,3], James Dunlop[4], Alex Eslinger[3], Prakhar Garg[1,11], Tom Hemmick[1], Alexander Jentsch[4], Alexander Kiselev[4], Henry Klest[1], Samo Korpar[6], Peter Križan[6], Jeffery Landgraf[4], Saverio Minutoli[9], Charles-Joseph Naïm[1], Mikhail Osipenko[9], Brian Page[4], Sanghwa Park[8], Matt Posik[7], Rok Pestotnik[6], Prashanth Shanmuganathan[4], Nikolai Smirnov[11], Bernd Surrow[7], Makoto Tabata[10], Silvia Dalla Torre[5], Zhoudunming Tu[4], Thomas Ullrich[4], Jan Vanek[4], Anselm Vossen[2,3], Craig Woody[4], and Zhengqiao Zhang[4]

[1]Stony Brook University, Stony Brook, New York 11794, USA
[2]Duke University, Durham, North Carolina 27708, USA
[3]Jefferson Lab, Newport News, Virginia 23606, USA[1]
[4]Brookhaven National Laboratory, Upton, New York 11973, USA
[5]INFN, Sezione di Trieste, Trieste, Italy[2]
[6]Ljubljana University and J. Stefan Institute, Ljubljana, Slovenia[3]
[7]Temple University, Philadelphia, Pennsylvania 19122, USA
[8]Mississippi State University, Mississippi State, Mississippi 39762, USA
[9]INFN, Sezione di Genova, Genova, Italy
[10]Chiba University, Chiba, Japan[4]
[11]Yale University, New Haven, Connecticut 06520, USA

March 22, 2023

[1]Engineering support by the EIC project
[2]INFN Trieste and INFN Genova authors committed only to the design and R&D phase
[3]Expert input only, no institutional commitments
[4]Expert input only, no institutional commitments

Abstract

The ePIC detector is designed for Interaction Point 6 (IP6) at the future Electron-Ion Collider (EIC) at Brookhaven National Laboratory (BNL). It is a multi-purpose detector aiming to provide large acceptance, good resolution, and strong particle identification capabilities in order to deliver the full physics program of the EIC. In this document, we present the Conceptual Design Report (CDR) of a proximity-focusing Ring Imaging CHerenkov detector, pfRICH, for the electron endcap region. It represents a comprehensive report of the technical progress made on the pfRICH design since October 2022, when the concept was first formulated for ePIC. The design is based in parts on work conducted in 2021 in the context of one of three EIC Project Detector proposals. The pfRICH meets or exceeds all the requirements expressed in the Yellow Report. It features minimal material budget, easy pattern recognition, large acceptance, and serves simultaneously as time-of-flight detector for the backwards region. This CDR is written in view of the comparative process to select the design and technology for the backward RICH for the ePIC detector, conducted in March 2023.

Contents

Executive Summary

We present the conceptual design of a proximity-focusing Ring Imaging CHerenkov (pfRICH) detector designed to provide the needed particle identification capabilities in the backward (electron-going direction) region of the ePIC detector. The pfRICH consists of a tiled aerogel radiator with an average refractive index of $\langle n \rangle \sim 1.045$, separated from an array of photosensors by a proximity gap of approximately 45 cm. The detector vessel has a cylindrical shape, coaxial to the electron beam line with the aerogel tiles located upstream (towards the vertex) of the vessel and the photosensors on the downstream side. The photosensors cover the full potential detector acceptance, which spans the pseudorapidity range of approximately $-3.5 \leq \eta \leq -1.5$. The proposed photosensors are large-size (10 cm $\times$ 10 cm active area) Micro-Channel Plate Photomultiplier Tubes, also known as High Rate Picosecond Photon Detectors (HRPPDs), manufactured by Incom[1]. HRPPDs are characterized by fine time resolution, better than $\sim$50 ps for single photon detection. In addition to e/π and π/K/p identification based on ring imaging, this feature will allow the pfRICH to provide a time-of-flight (ToF) measurement of $\sim$20 ps or better by combining information from the single photon hits associated with the aerogel rings and multi-photon clusters produced by charged particles traveling through the fused silica windows of the photosensors. This will not only add low-p_T PID of hadrons and electrons to the backwards region, but will also provide a time reference (t_0) for the barrel and forward endcap ToF detectors.

The expected pfRICH momentum range for hadron identification and electron-hadron separation is given in Table 1. The identification range is defined as the momenta for which the signals expected from the competing particle species are separated by at least 3 times the track-level Cherenkov angle resolution (3σ separation). Positive kaon identification momentum range based on ring imaging with the aerogel radiator is quoted. The lower limit will be substantially improved once ToF information is fully accounted for to distinguish between the low momentum kaons and protons. This performance matches the physics requirements outlined in "Science Requirements and Detector Concepts for the Electron-Ion Collider: EIC Yellow Report (2022)" [1].

Table 1: Expected pfRICH momentum reach.

competing particle species	separation range (GeV/c)
e *vs* π/K/p	$\sim$0.2 $\div$ $\sim$2.5
K *vs* π/p	$\sim$ 2.0 $\div$ $\sim$9.0

[1]Incom, Inc., 294 Southbridge Rd, Charlton, MA 01507, USA

Chapter 1

Introduction

In this Conceptual Design Report, we propose a particle identification (PID) device, a proximity focusing Ring Imaging CHerenkov detector (pfRICH), in the backward region[1] of the ePIC experiment. Our proposed design features a tolerable material budget in front of the endcap crystal electromagnetic calorimeter, easy pattern recognition, large acceptance with a uniform level of performance over the whole available pseudorapidity range and 2π coverage in the azimuthal angle. This design can also simultaneously function as a high resolution timing device and, provided a gas other than nitrogen is chosen in the future, as a threshold gas Cherenkov counter.

In order to fulfill the science mission at the EIC, an experiment with a wide range of PID capabilities in the backward region is indispensable. The large acceptance in the backward region, combined with comprehensive PID capabilities are among the most-important ePIC detector features. Having extended coverage in acceptance to reconstruct scattered electrons near $Q^2 = 1$ GeV^2, combined with the ability to acquire very high (99%) electron purity via PID enables ePIC to improve drastically on the capabilities of H1 and ZEUS at HERA. We will detail the need for a pfRICH in the ePIC detector in Chapter. 1.1.

The proposed HRPPD photosensors will serve two major functions when fully integrated into the pfRICH: i) detection of Cherenkov photons from the aerogel radiator to determine the emission angles for ring imaging, and ii) detection of Cherenkov photons produced in the quartz windows of these sensors to provide a timing reference better than ∼20 ps for ePIC ToF subsystems. The high resolution timing capability eliminates the need for a separate timing detector in the backward region, helping to minimize the material budget in front of the electromagnetic calorimeter. Further details will be discussed in Chapter 1.2.

For the rest of this Conceptual Design Report, we first present an overview of the pfRICH detector and its subsystems in Chapter 1.3, followed by a detailed technical discussion on the design and integration in Chapter 2. The magnetic fields and particle fluxes expected in the pfRICH region, and their consequences, are detailed in Chapter 3. The detector and physics performance are given in Chapter 4 and Chapter 5, respectively. The cost, schedule, and workforce details are presented in Chapter 6, and finally, an R&D outline is provided in Chapter 7. We attach an Appendix at the end of this report for supplementary material.

[1] backward region refers to the electron-going direction in our convention

1.1 The need for a PID detector in the backward region

Particle identification in the backward region enables the study of a broad range of diverse physics topics. It is important for both the identification of the scattered electron as well as the hadronic final state.

As sketched in Fig. 1.1, hadrons in the backward region generally originate from collisions probing low x, with Q^2 held constant, or higher Q^2 at fixed x. The pfRICH covers the backward region of $-3.5 \leq \eta \leq -1.5$, which is the smallest η region accessible within the central detector. This phase space is of great interest for studies in both e+p and e+A collisions. In e+A collisions this is the kinematic region where the onset of gluon saturation is expected. Saturation generally describes novel QCD phenomena originating from the overlap of the gluon wavefunctions, which is thought to happen at low x where gluon densities are high. Saturation effects are thought to be enhanced in e+A collisions by a factor $A^{1/3}$. This is also a range that has never been explored by polarized e+p experiments before.

For semi-inclusive DIS (SIDIS) measurements in particular, particle identification is essential. As an important example, the determination of the polarized sea quark distributions requires measurements of identified kaons in the backward region. This, and other channels, are described in more detail in the EIC Yellow Report [1].

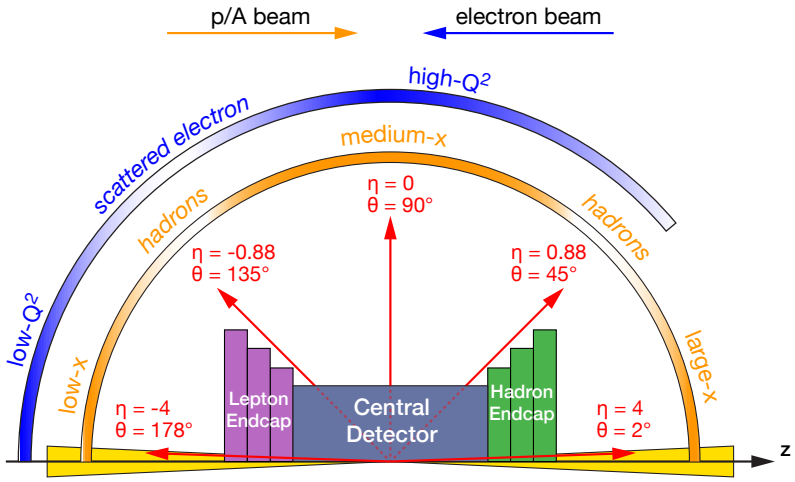

Figure 1.1: Schematic illustration of EIC detector hemispheres showing the distribution of the scattered lepton and hadrons for different $x - Q^2$ regions over the detector polar angle coverage.

Studies of physics requirements in the Yellow Report define the particle identification (PID) requirements in the backwards region. Driven mostly by SIDIS measurements, the requirements in the pseudorapidity range $-3.5 \leq \eta \leq -1.5$ demand 3σ separation or better of $\pi/K/p$ for momenta $p < 7$ GeV/c . In this context, it is also useful to look at Fig. 1.2 which shows the momentum distributions of the most abundant particles for different pseudo-rapidity bins in the backward region for beams of 5 GeV electrons on 41 GeV protons and 18 GeV electrons on 275 GeV protons. This illustrates that the loss of PID

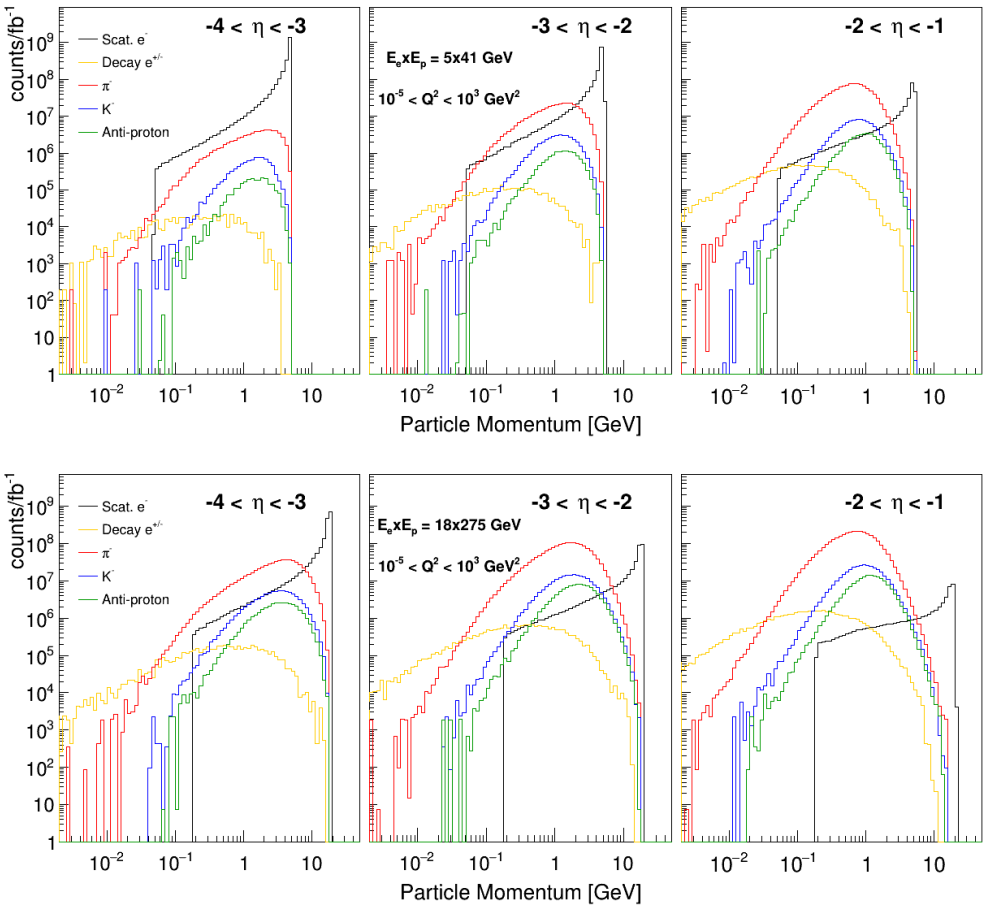

Figure 1.2: The momentum distribution of the relevant particles for different pseudo-rapidity bins in the backward region for beams of 5 GeV electrons on 41 GeV protons (top) and 18 GeV electrons on 275 GeV protons. The covered Q^2 region extends from 10^{-5} to 10^3 GeV^2 and no additional kinematic cuts have been applied.

above 7 GeV/c has only a minor effect. The plot also shows the evolution of the e/h ratio (black vs. red, blue, and green curves). It is worth noting that a more differential study of the momentum distributions in different $x - Q^2$ bins, employing standard SIDIS cuts, showed that there is no unique phase space that is accessed by particles with $p > 7$ GeV/c in the pfRICH acceptance.

While no concrete requirements on the e/h ratio for PID detectors alone were enumerated in the Yellow Report, [2] it is clear that at lower momenta the electron ID capabilities of the backward EM calorimeter will not be sufficient to achieve the overall required electron purity of 99%. The extra suppression power can only be met by additional PID capabilities from the RICH detector, especially in the region below 3 GeV/c where the hadron

[2]The Yellow Report only discusses the need for the overall hadron suppression in the backward region of 10^4. At high momenta this suppression is predominantly provided by the EM calorimeter but at lower momenta this will not be possible.

distributions are at their maximum. To access low Q^2, it is essential to provide PID in this region which includes $Q^2 = 1$ up to $\eta = -2$ and lower Q^2 up to the quasi-real photoproduction regime further backward. As low-Q^2 is correlated with low-x (at high inelasticity), e/h separation is essential to access the lowest x for the reasons outlined above. It is also important to provide a bridge between the phase space covered by the central detector and the far backward detectors that detect events with $Q^2 \gtrsim 10^{-3}$ GeV^2. The reasons outlined in this section make the backwards PID system essential for the EIC physics program.

1.2 The case for Time of Flight in the backward region

The original baseline design of the ePIC detector included ToF detectors based on AC-LGAD technology in the forward, backward, and barrel regions. Their purpose was to provide PID in the momentum region below the aerogel threshold ($\lesssim 1$ GeV/c). While physics measurements exist that require PID at low momenta in the forward and barrel region, there are no such arguments for the backward range. The main argument for the presence of an AC-LGAD based ToF for $\eta < -1$ was to aid in providing the start time, t_0, for all ToF measurements in ePIC, mainly by utilizing the scattered electron.

After serious concerns raised by the EIC Project about the heat dissipation of the AC-LGAD ToF system that would affect the calibration and performance of the backward electromagnetic calorimeter, ePIC's Global Design and Integration group (GD/I) was charged to evaluate the need for an AC-LGAD ToF layer in the backward endcap and to suggest alternative solutions. After involving physics and detector working groups, as well as consulting several sub-system experts, the GD/I group came to the following conclusion:

"We recommend not to include the backward AC-LGAD TOF as the baseline choice for the backward TOF. [...] We believe a fast RICH photo-sensor, specifically the LAPPD, provides a better-integrated detector solution for the backward t_0 measurement. We believe this measurement can be realized and augmented using 3D vertex-time correlation."

Following this recommendation, ePIC management decided to take the AC-LGAD ToF out of the backward endcap and made the LAPPD the new baseline sensor for the backward RICH.

This implies that a pfRICH with LAPPD readout will need to provide the necessary t_0 with a resolution of $\sigma_t < 25$ ps. This, in conjunction with vertex-time correlations (see Sec. 4.3.1), will provide a high quality t_0 for events where the scattered electron is detected in the backward region. It will also provide input in cases where the t_0 has to be derived from a bootstrap method using all timing detectors in the full ePIC coverage.

1.3 Overview of the proximity focusing RICH

The ePIC pfRICH was designed as a conceptually simple detector, based on proven principles, providing a high degree of performance that is practically uniform over the whole available angular acceptance in η and ϕ, and allowing the use of straightforward event reconstruction algorithms. Key details of the design and the rationale behind particular

choices follow.

A generic proximity focusing RICH detector is based on a very simple set of principles, illustrated in Fig. 1.3. A charged particle passing through a thin layer of radiator (often aerogel with an appropriate refractive index) with a velocity higher than the speed of light in this medium emits Cherenkov light (photons) at an angle which is solely determined by the particle mass, momentum, and refractive index of the radiator. The 3D momentum of the particle is typically provided by a tracking system. If the average refractive index of the radiator is also known, measurements of the Cherenkov light emission angle can determine the particle mass, thus allowing identification of particle species with different masses, e.g. distinguishing electrons, pions, kaons, and protons.

In order to measure the emission angle, a pixelated photosensor matrix is installed at a certain distance (a proximity gap) from the radiator. The single photon 3D detection point on this matrix and a known (up to the radiator thickness) 3D emission point where the particle crossed the radiator volume provides a 3D vector in space. The relative angle of this vector with respect to the known (from tracking) particle direction at the location of the emission point is the measured single Cherenkov photon emission angle. Averaging all photons emission angles associated with a track provides the track-level quantity for particle identification.

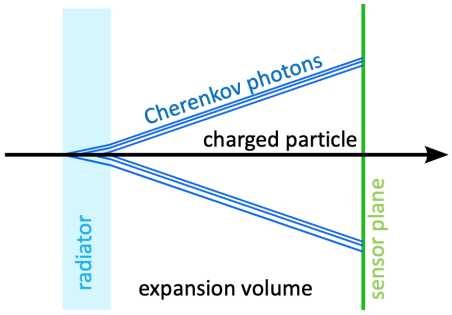

Figure 1.3: A schematic setup of a typical proximity focusing RICH. See the text for more details.

Apart from the tracker angular (and to a lesser extent momentum) resolution, the accuracy of this particle identification procedure is mostly determined by the length of the expansion volume, the photon emission point for a given finite radiator thickness, spatial resolution of the pixelated sensor matrix, the wavelength dependency of the medium refractive index, and the number of radiated Cherenkov photons. The intrinsic uncertainties associated with these features result in the uncertainty of the Cherenkov photon emission angle, which propagates to the single photon angular resolution. Therefore, as a rule of thumb, a good proximity focusing RICH should have: (1) a large proximity gap, (2) a thin radiator, (3) high spatial resolution in the photosensor matrix, (4) a weak $n(\lambda)$ dependency in the photosensor effective quantum efficiency (QE) range, and (5) a sufficient number of detected photons per track.

The layout of the proposed ePIC pfRICH detector is shown in Fig. 1.4. It consists of a 1.3 m diameter and ∼54 cm long cylindrical vessel with the upstream, inner, and outer walls made from a lightweight honeycomb carbon fiber sandwich and a rear plate machined from a single piece of a 1/2" thick aluminum alloy. Additionally, forty-two 2.5 cm thick aerogel tiles of a trapezoidal shape are installed in individual opaque compartments in a container mounted on the upstream side of the vessel. A thin acrylic filter is installed immediately after the aerogel container. More details are given in Sec. 2.2. The vessel is continually flushed with dry purified nitrogen. Sixty eight HRPPD photosensors are installed in individual slots in the rear aluminum mounting plate with their quartz windows facing the aerogel. Inner and outer conical mirrors cover the cylindrical sides of the vessel in order to increase the η acceptance of the Cherenkov photons produced in the aerogel

radiator. Readout boards equipped with four 256-channel EICROC ASICs are mounted on the rear ceramic anode plates of each of the HRPPDs for a total of 1024 channels per sensor. Given an HRPPD active area of 108 mm x 108 mm, this corresponds to 32x32 pixels per sensor with a pitch of 3.375 mm.

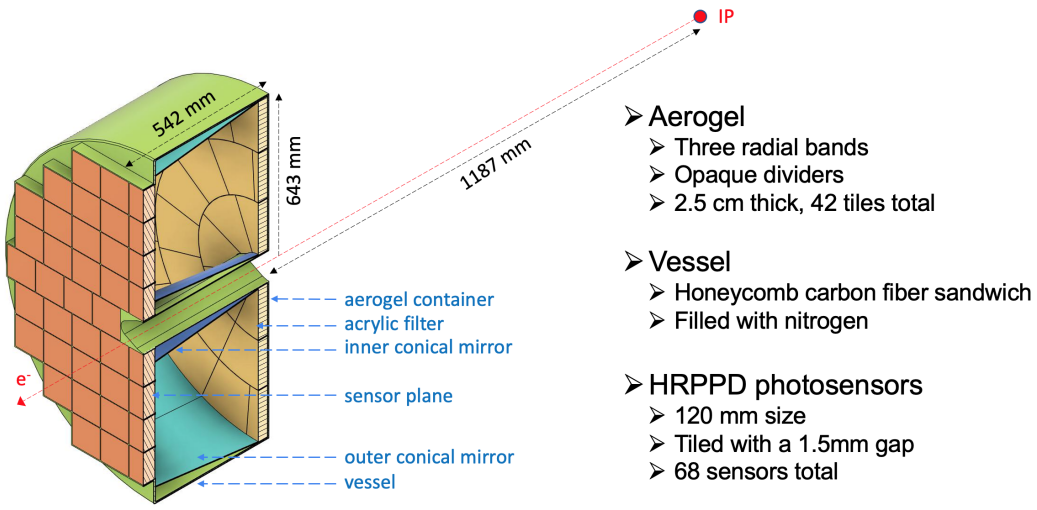

Figure 1.4: The proposed pfRICH detector. See the text for more details.

Following the guidelines of generic proximity focusing RICH optimization outlined earlier in this section, the pfRICH design was optimized in the following ways: (1) the proximity gap length is maximized as much as possible within the volume available in ePIC by reducing to an absolute minimum the space allocated for the HRPPDs and the onboard electronics; (2) the radiator thickness is taken to be small enough to reduce the contribution to the angular resolution to below ∼5 mrad, yet produce enough photons per track; (3) the HRPPD pixelation is chosen such that it contributes at most ∼2 mrad to the angular resolution; (4) the acrylic filter cuts off all UV light produced in the aerogel below $\sim$ 300 nm, where the $dn/d\lambda$ dependency is strongest; (5) the radiator thickness is still sufficient to produce an average number of photons per track close to the saturation angle of ∼295 mrad equal to $\langle N_{pe} \rangle \sim 12$.

Chapter 2

pfRICH Design and Integration

2.1 Overall mechanical design considerations

The initial physical dimensions for the pfRICH were sourced from the EIC geometry database [2]. According to the latest data, the pfRICH has an envelope that spans 54.1 cm in length, starting at -118.6 cm from the IP and extending back to -172.7 cm at its furthest extent. These two basic numbers were strictly adhered to.

Contrary to that, a detailed study of the surrounding construction elements (the DIRC frame and the beam pipe) revealed the fact that the numbers provided in the database can only be taken as a very conservative guidance, at best. Therefore when designing the vessel together with the EIC project mechanical engineer, we only considered the actual physical constraints, following from the CAD drawings of the respective neighboring components. The pfRICH vessel was, in the end, designed to provide a clearance of 5 mm to the electron beam pipe flange (see Fig. 2.2 further in the text) during the installation procedure, and about an 8 mm clearance to the DIRC frame both during the installation and at its final location, see Fig. 2.1.

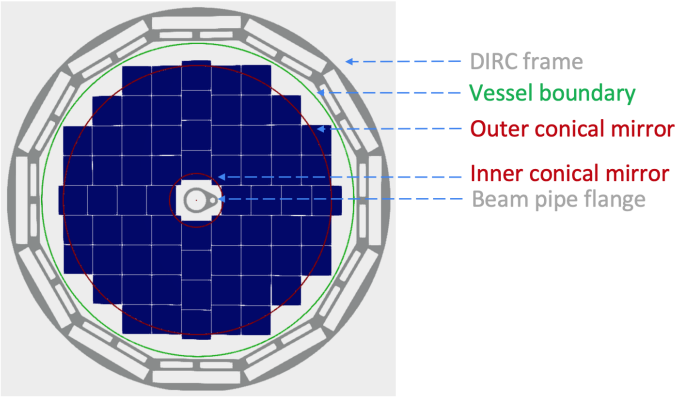

Figure 2.1: pfRICH photosensor plane tiling scheme, which also shows the geometry of the beam pipe flange downstream of the detector and a crosscut view of the DIRC frame.

Various aspects relevant to the mechanical design of the specific components follow.

Aerogel Wall

The wall's frame is intended to be made from thin carbon fiber. The design assumes that individual aerogel tiles will be placed in their respective compartments and fixed in place by either a few Plexiglas sheets covering the whole ∼1.3 m diameter container on the downstream end, or by a set of thin filaments. A lightweight, standalone aerogel wall can then

be assembled separately and inserted into the vessel front wall disk as a whole during the assembly procedure. Further details are given in Sec. 2.2.

Sensor Plane

The sensor wall is based on the projected HRPPD design, which features a 12 cm x 12 cm front face with notched corners for installation. The tiling scheme is then constrained by the inner and outer radii available for the pfRICH vessel. The inner radius is defined by the oblong beam pipe flange, see Fig. 2.2. As this figure shows, the flange shape requires that the tiling be offset by 40 mm at the central row on the right hand side along the electron-going direction. The outer radius is defined by the DIRC frame, and while considering installation clearances, is defined as 64.3 cm.

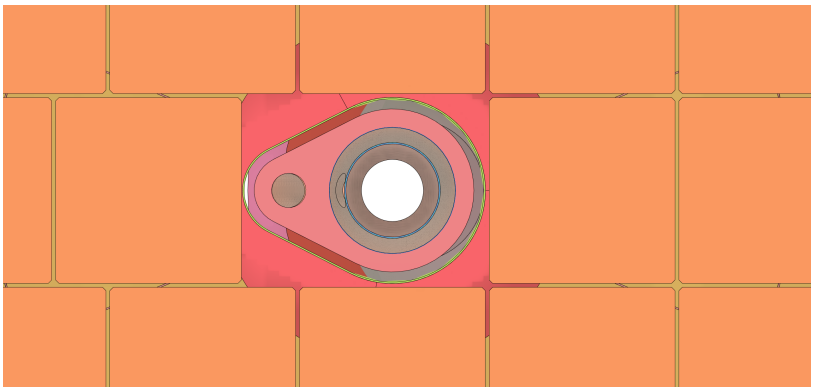

Figure 2.2: View from beam pipe flange showing clearance in the tiling scheme. 120 mm x 120 mm large HRPPD photosensors surrounding the flange are shown in orange. The central row is shifted sideways by 40 mm to avoid a conflict with the smaller incoming hadron beam pipe flange.

Once the size of the tiles, the inner radius, and the outer radius are defined, the tiling scheme can be created. In this case, the tiles are spaced at 121.5 mm. This 1.5 mm allows for a 1.0 mm thick wall for the supporting grid with an additional 0.5 mm of tolerance to allow for size discrepancies in HRPPD manufacturing.

The sensors are supported by a grid structure that allows each HRPPD sensor to be inserted individually from the downstream end. This grid structure is independent of the outside containment volume that will be described in a subsequent section. The grid has 1.0 mm spacer sections that go up all four sides of the sensor block and has a feature on the most upstream end that supports the front (window) side of the sensor. This feature is a 12 mm wide and 3 mm thick grid. Although this would appear to block some portion of the sensor window, there is a 6 mm wide dead area on the perimeter of the sensor due to the way the HRPPD is designed. Therefore, supporting the sensors in this manner has very little effect on the performance of the detector. On the downstream end, the sensors are held in by regular threaded hardware and washers that press the sensor to the grid frame via a soft gasket, providing both gas and light tightness.

Outside Containment Volume

The outside containment volume houses several key features of the pfRICH detector. Following the ideas developed for the construction of the sPHENIX TPC [3], the most current design uses honeycomb carbon fiber sandwich layers of ∼1/2" thickness (outer wall) and ∼1/4" thickness (front and inner walls) as the primary material for the containment volume.

The primary purpose of the containment volume is to support the entirety of the pfRICH structure within the hpDIRC frame. To that end, the current concept is to use conical features on the upstream end that locate the detector subassembly precisely. On the downstream end, the subassembly would be held radially by using typical hardware (bolts/washers) on mounting points that are extended from the hpDIRC frame, see Fig. 2.3.

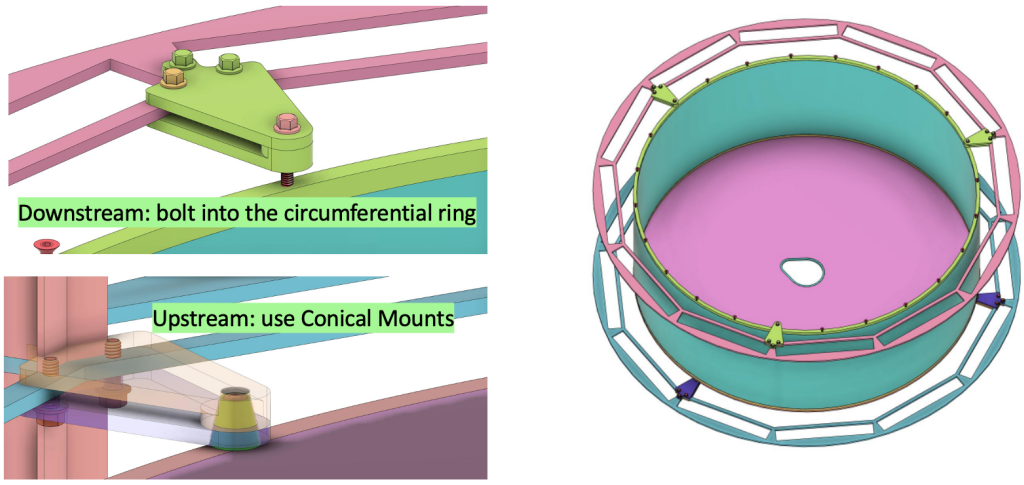

Figure 2.3: pfRICH vessel mounting scheme. Bottom left and top left: see the text for more details. Right: location of the upstream and downstream mounting fixtures on the vessel.

Secondarily, the containment volume keeps the system light tight and contains the gaseous volume. On the upstream end, the aerogel wall fits within the containment volume to create a light and gas tight seal. Moreover, on the downstream end, a similar sealing scheme is foreseen for the interface between the inner and outer cylindrical walls and the rear aluminum plate holding the photosensors.

Lastly, the containment volume needs to support the mirrors within the system. The baseline design has two conical mirrors: one near the beam pipe, which is conical in shape and expands as it goes downstream, and the other mirror on the outer radius – also conical in shape – that is wider upstream than it is downstream.

There is a special cutout on the inner mirror due to the beam pipe flange shape of the inner wall of the containment volume, see Fig. 1.4. Since this cutout is needed to install the detector, the loss of mirror in this area is accounted for in the GEANT simulation and determined to be a reasonable trade-off. The outer mirror, in contrast to the inner mirror, will be bonded to the containment volume by utilizing support struts which will fill the volume between the mirror and the outer containment vessel. These support struts will be optimized when the containment volume is analyzed. The mirror radius on the

upstream end will be approximately 62 cm and taper down to 57 cm on the downstream end. Azimuthal segmentation of this mirror (three to six sectors) will be determined at a later stage, based on the manufacturer feedback.

Detector Installation

The pfRICH detector installation is highly dependent on the surrounding systems. Initially, it was thought that the pfRICH needed to be split apart and installed in halves. One of the driving factors behind this thought process was that the detector needed to clear the downstream beam pipe flange and be of the smallest installed diameter (to get the best acceptance towards the beam pipe) when in its installed position. However, the added complexity of splitting the detector in half would mean that there would be compromises elsewhere in the detector. The loss of acceptance near the beam pipe is anyway partially recovered by the inner mirror.

Therefore, after discussions with the EIC lead integration engineer, it was determined that the detector could have the beam pipe flange shape (with an additional 5 mm of clearance all the way around) cut straight through the pfRICH assembly. This way, the entire detector can be fully assembled and instrumented before being inserted into place.

Since the downstream EEMCAL has to be taken out as a whole piece, this means that the only way any maintenance can be done on the pfRICH is while the detector is rolled out into the assembly hall. Therefore, a similar fixturing system and rails to what is used to remove/install the EEMCAL can also be used to reach in and remove the entire pfRICH.

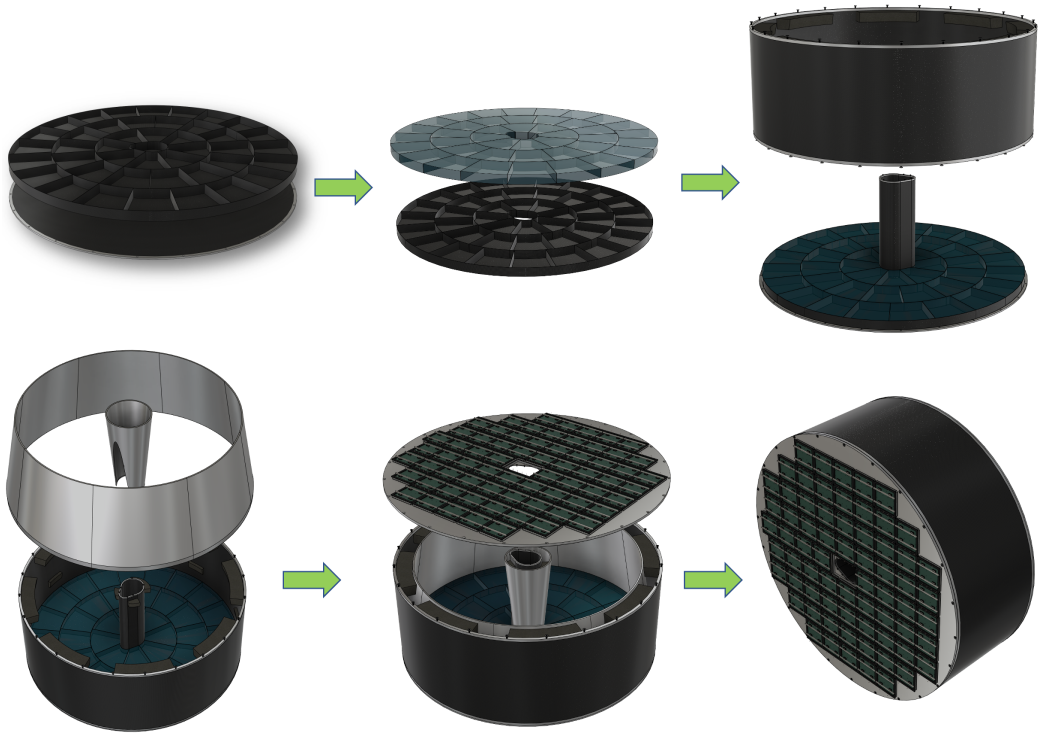

Figure 2.4: pfRICH assembly procedure. See the text for further details.

Detector Assembly

As stated, the entire pfRICH assembly is being designed so that it can be assembled in one piece. The general order in which this has been designed is as follows: (1) pre-assemble the aerogel wall, (2) pre-assemble the outer containment volume with the mirrors, (3) place the circular retaining disk (aka the front vessel wall) down, (4) add the aerogel wall on top of the retaining disk, (5) place the outer containment volume over the aerogel wall, (6) fasten the retaining disk to the outer containment volume (locking the aerogel wall in place and adding the conical locating features to the hardware), (7) place and fasten the aluminum grid assembly to the outer containment volume, (8) install and fasten the individual HRPPD modules into the back of the grid assembly, (9) install and fasten the fully assembled pfRICH detector inside of the DIRC frame, (10) install the services. See also Fig. 2.4 for a pictorial description of the procedure.

Future Considerations

Beam pipe bakeout temperatures in excess of 100 C will require thermal insulation in the few cm radial gap between the beam pipe and the pfRICH vessel in the installation location.

2.2 Aerogel radiator

The ePIC pfRICH will be equipped with aerogel produced by Chiba Aerogel Factory Co., Ltd. [4] with a nominal refractive index, n, of 1.045 and a thickness of 2.5 cm. The aerogel will be cut into three trapezoidal shapes, matching the segmentation shown in Fig. 2.5 (left), using a water jet technique.

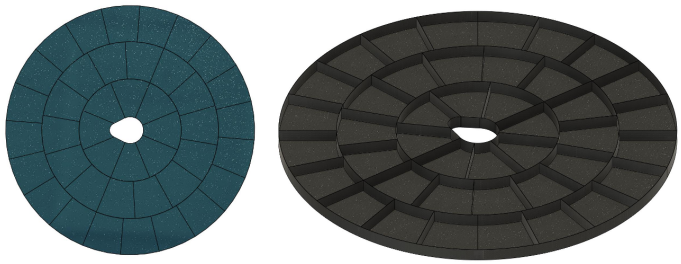

Figure 2.5: The pfRICH aerogel wall will be segmented in three radial bands, populated by 8, 14 and 20 trapezoidal shape tiles, respectively.

This type of aerogel should replicate the performance of the material with the same refractive index used in the Belle II experiment [5], and in particular be very transparent in the near UV range, with an absorption length and Rayleigh scattering length in excess of 5 mm down to ∼250 nm. The Belle II aerogel GEANT parameterization, with a refractive index of 1.045, was used in all Monte-Carlo simulations presented in this report.

Another option for the pfRICH would be using aerogel similar to the 2.5 cm x 15 cm x 15 cm sized tiles with $n = 1.040$ that are currently being produced for J-PARC [6]. In this case four, rather than three, radial bands (and consequently four different shapes) would be required.

In a meeting with the manufacturer held in December 2022, and a follow up exchange, it was agreed that Chiba Aerogel Factory will begin producing smaller sized aerogel test samples for ePIC RICH detectors in April 2023. These samples will be appropriate for bench top evaluation as well as the pfRICH detector prototype beam tests currently planned for

spring 2024, once the first five new-generation HRPPD tiles are produced.

In the experiment, the aerogel tiles will be installed in a segmented container with 500 μm thick walls and slots holding individual tiles (see Fig. 2.5 right). The container walls will be opaque to suppress stray photons leaking out of the aerogel tile walls, which are not expected to be of a high optical quality.

The pfRICH configuration, simulated for the purposes of this document, included a thin acrylic filter with a 300 nm wavelength cutoff to suppress the UV part of the Cherenkov spectrum. In case this layer is not used in the final setup, then, similar to what was done in the Belle II experiment, the tiles will be retained by a thin fishing line filament on the downstream side to prevent them from falling out of the container.

Given the radial and azimuthal segmentation, the pfRICH detector will require 42 aerogel tiles total. In the course of the 2023-2024 calendar year, an optical stand will be set up at Temple University to provide quantitative measurements of the aerogel characteristics.

2.3 Photosensors

An improved version of the Micro-Channel Plate Photomultiplier Tubes (MCP-PMTs) manufactured by Incom Inc. [7], the so-called High Rate Picosecond Photon Detectors (HRPPDs), will be used as the photosensor solution. Their formfactor and other characteristics will be tuned to EIC needs over the next two years as part of the EIC-Incom Project Engineering Design (PED) contract, which is currently (March 2023) under preparation. The sensor dimensions will be 120 mm x 120 mm, with a 108 mm x 108 mm fully efficient active area in the center (80% geometric efficiency) and will have slightly tapered 5 mm thick UV-grade quartz windows, side walls thinned to 3 mm, and 3 mm thick multi-layer ceramic anode base plates. A DC-coupled variety of these sensors will be used, with the inner side of the anode base plate patterned into 32x32 square pixels, corresponding to 1024 channels per sensor, and a pitch of 3.375 mm.

The sensors will be equipped with a UV-enhanced high quantum efficiency (QE) bialkali photocathode, with peak values exceeding 30% at 350 nm [8], that was developed by Incom under the US Department of Energy (DOE) Small Business Innovation Research (SBIR) contract "Development of Advanced Photocathode Materials for LAPPD" [9]. This type of QE spectrum allows one to maximize the light output from Cherenkov photons produced by a charged particle crossing the quartz window, while also providing sufficient sensitivity in the optical range. The former is critically important for providing a required timing reference for the ePIC experiment on the level of 10-20 ps. The latter is necessary to maintain a large enough yield of Cherenkov photons from the aerogel for ring imaging purposes.

The HRPPDs will be fitted with a pair of 600 μm thick MCPs with a pore diameter of 10 μm, open area ratio in excess of 70%, and bias angle of 13 degrees in a conventional chevron configuration. These will be operated at an amplification voltage of $\sim$1 kV to comfortably achieve an overall detector gain above 10^6 if needed. Transfer gaps and voltage settings will be tuned to provide a high resolution timing measurement, with an expected single photon Transit Time Spread (TTS) of $\sim$50 ps.

As confirmed by recent measurements performed at Argonne National Laboratory (see Sec. 3.1), when placed in a solenoidal magnetic field of 1.3 T (roughly the value to be

expected at the location of the pfRICH in ePIC), the above photosensors basically work in a "binary" mode, where a single photon leaves a substantial signal in only one pad and charge sharing between neighboring pads is minimal. The spatial resolution in this case is determined by the canonical expression of pitch/$\sqrt{12}$ and timing resolution is maximized. The same measurements confirmed that for magnetic fields of this magnitude, oriented at an angle of up to 12 degrees to the sensor normal (the condition expected at a radius of ∼600 mm in the pfRICH sensor plane), the detector gain can be fully recovered by increasing the amplification voltage by ∼200 V.

The anode base plates will be built from multi-layer Low Temperature Co-fired Ceramic (LTCC) manufactured by Techtra [10] in Poland. They will have a custom design, matching the uniform 32 x 32 pixelation on the inner (vacuum) side of the sensor, short shielded traces inside of the ceramic stack, and a pattern on the outer side matching the readout PCB design. The first 3" sized samples of the required type were produced in February 2023 (see Fig. 2.6) and are being evaluated for flatness, mechanical and electrical properties, and vacuum tightness at Incom Inc. A full size prototype will be built by summer 2023.

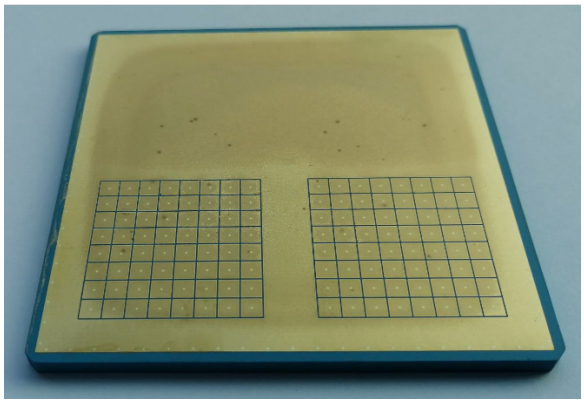

Figure 2.6: First 3" size multi-layer ceramic base plate prototype produced by Techtra (Poland) for Incom according to BNL design. These prototypes have two 8x8 pad fields with a pitch of 3.375 mm, and a set of embedded shielded traces in four different geometries, for a 50 Ohm impedance matching evaluation.

Connections to the ASIC readout board will be made using Samtec high density compression interposers and, in the easiest configuration, will be comprised of sixteen off-the-shelf 10 x 10 contact Z-Ray plates with a pitch of 1.0 mm [11] bump-bonded to the readout PCB on one side and bolted to the ceramic plate using the embedded threaded fixtures. The ceramic plates will naturally have sixteen matching 10 x 10 pad spots, where the inner 64 spots (8 x 8 contacts) will be used to connect the signal pads and the outer 36 spots for additional grounding. This design represents a compact, integrated photosensor and eliminates any permanently mounted irreplaceable electronic components on the rear side of the HRPPDs. The total estimated load produced by the spring loaded contacts is equivalent to roughly 3 kg per interposer and acts as a local force that does not produce additional pressure on the sealed vacuum volume that could cause a sensor collapse.

Six high voltage pins will be located on the rear side of the sensor (ground, four MCP HV leads and the photocathode HV). Sensors will be mounted "face down" into their respective slots in the aluminum mounting plate during the installation procedure and fixed to the mounting plate using soft radiation hard gaskets to provide both light and gas tightness in situ. Electrical isolation will be achieved using 3 mil kapton sheets. The sides of the sensor quartz windows will be blackened by the manufacturer in order to suppress any light leaks.

2.4 Readout electronics

Each sensor will be equipped with four 256-channel EICROC ASIC cards [12], designed by the OMEGA group [13], each serving one quadrant of the sensor. EICROC ASICs will be built via a 130 nm technology process, with an expected power consumption of 1-3 mW/channel [12]. They will provide a Time of Arrival (TOA) and an ADC measurement with a dynamic range of 1 pC for each pixel, which should be sufficient for both single photon hits (imaging) and multi-photon hits (timing) at a moderate HRPPD gain of a few times 10^5. The ASICs will have a configurable preamplifier and a Constant Fraction Discriminator (CFD) and will be able to measure the TOA with a resolution better than 20 ps per pixel provided the detector capacitance does not exceed 5-10 pF, leading edge length of the HRPPD signal is below 1 ns and collected charge of a few dozens fC can be achieved by tuning the MCP gain [13]. These ballpark parameters seem to be easily within reach for pfRICH HRPPD sensors.

The ASICs will be bump bonded to the readout PCB in a "flip-chip" fashion to minimize the parasitic capacitance of the traces inside of the PCB stack. Preliminary estimates show that in such a scheme, where four 16 x 16 primary pixel arrays with a pitch of 3.375 mm are first "compressed" to a 1.0 mm pitch inside the ceramic base plate and then further reduced to a 500 μm pad size in the readout PCB stack in order to ultimately match the EICROC ASIC pitch, the combined pad and trace capacitance should not exceed 10 pF. This is well within the operating range of the ASICs, provided the initial HRPPD gain can be maintained at a level of roughly 50 fC, corresponding to the single photon pulse Most Probable Value (MPV).

Each ASIC will be connected via a dedicated copper link to its respective readout unit (RDO), located on the outer circumference of the rear side of the pfRICH vessel. Each RDO will serve 16 EICROC ASICs, for a total of 17 RDOs. The RDOs will then be connected to a single Data Aggregation Module (DAM). The DAM board is envisioned to be a FrontEnd LInk eXchange (FELIX) board [14] installed in the DAQ room via a high speed optical uplink capable of at least 10Gb/s throughput. The RDOs will be the standardized ePIC PCBs with a Xilinx UltraScale+ FPGA. The RDO will aggregate the ASICs data and implement the ePIC DAQ configuration, timing and streaming data protocols. The RDO should deliver timing signals synchronized to the beam crossings with jitter $<$ 5ps.

Preliminary rate estimates [15] at maximum EIC luminosity of $10^{34}\text{cm}^{-2}\text{s}^{-1}$ give physics collision rates of 5 Gb/s, hadron beam gas rates of 0.6 Gb/s and electron beam gas rates of 21 Gb/s. Noise from the HRPPD Dark Count estimated at 2 kHz/cm^2 lead to 1 Gb/s leading to an expected throughput $<$ 30Gb/s. Under these estimate the RDO to DAM data will utilize $<$20% of the RDO capacity, and the $<$30% of the DAM readout capability.

2.5 Power distribution

High Voltage (HV) and Low Voltage (LV) modules will be located on the electronics platform, about 15 meters away from the pfRICH detector, in a low Total Ionizing Dose (TID) environment. Therefore standard off-the-shelf units can be used.

2.5.1 High Voltage system

The high voltage system will consist of 340 individual stackable negative HV channels. Twenty three CAEN A1515BV 16-channel 1.4kV/1mA floating ground modules [16] will be used. They will be installed in a pair of CAEN SY4527 mainframes [17], equipped with additional 1200 W power module boosters.

Each of the twenty three modules will be connected to a patch panel installed on the rear side of the pfRICH vessel via individual 15 m long 37-wire high voltage cables. CERN-approved 52-pin Radiall cable connectors and receptacle parts will be used throughout the system. Soldered contacts on the rear side of the Radiall receptacles will be wired in such a way as to provide five individual stacked voltage levels and a ground reference to each HRPPD. The respective six outputs will be connected to the pins on the rear side of the HRPPDs via thin individual 18 kV rated 1.27 mm diameter Teflon coated 24AWG wires to minimize the dead material in front of the high precision electromagnetic calorimeter.

2.5.2 Low Voltage system

The EICROC ASICs will require 1.2 V low voltage power. Under the assumption of up to 3 mW/channel power dissipation this corresponds to 3 W power (or up to 2.5A current) per photosensor Front End Board (FEB). Accounting for other electronics components present on such a FEB, and providing a 20% safety margin, we estimate the total power consumption to be less than 300 W for the whole system. This number is used as input for designing the cooling system, see Sec. 2.6.

We will be using a single Wiener Mpod Mini LX crate with a Mpodc controller and four MPV4008I1 4-channel LV modules [18]. One Low Voltage channel will serve four FEBs. 15 m long 10AWG (power lines) and 20AWG (sense wires) cables will run between the electronics platform and a patch panel on the rear side of the pfRICH vessel. From there, thin 18AWG wires will bring power to the individual FEB cards.

Readout boards (RDOs), also located around the outer circumference of the pfRICH vessel, will be powered in a centralized way, following the prescription provided by the EIC project and / or ePIC Collaboration.

2.6 Cooling system

The pfRICH cooling system will consist of several off-detector components and a few on-detector thermal interfaces and assemblies. The primary heat dissipating components will be the ASICs, which are anticipated to produce just over 1 W each (4 W per module), or about 300 W for the 68 total modules. In addition to the ASICs, the sensors are anticipated to dissipate just under 1.5 W each or 100 W total. Conservatively, the total power output will be roughly 400 W. Following the geometry, each row of sensors will have its own pair of titanium cooling tubes directly over the ASICs. The pair of tubes that contact the same row of sensors will be in series, and all rows will be in parallel with each other. The tubes will be attached to aluminum plates with thermal epoxy and a gap pad between the plate and ASIC will maximize thermal contact (Fig. 2.7). Although aluminum tubes would offer superior thermal performance, titanium was selected to mitigate the risk

of corrosion and minimize the need for customization of off-the-shelf circulators. Using a stock tube of 0.25" OD and 0.218" ID and maintaining a minimal temperature gradient in the water allows the mass flow rate to be calculated. From there the Reynolds number and pressure drop can be determined, confirming the viability of the system. Additionally, a finite element analysis (FEA) can be preformed to confirm the water temperature difference and determine the thermal gradient across the various components (Fig. 2.7). With the described configuration, the sensors reach a maximum temperature of about 32 C in the analysis. It should be noted there are a number of assumptions made in the FEA, for example convection and radiation are not accounted for.

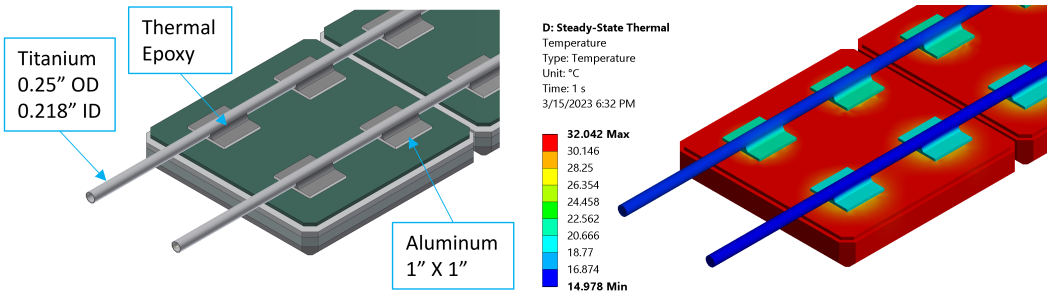

Figure 2.7: (Left) Schematic of the on-detector cooling assembly. (Right) Expected thermal gradiant across various sensor stack components.

The three primary off-detector elements of the cooling system are a Polyscience chiller, Chilldyne circulator, and a distribution panel. The Polyscience chiller will allow the water to be slightly colder than room temperature, or about 15 C, which is the lowest recommended temperature without nearing the dewpoint in the interaction region. The unit is also capable of flowing about 10 liters per minute (lpm), dissipating about 800 W at that temperature and maintaining the temperature within +/-0.1 C. The Polyscience chiller would be paired with a Chilldyne negative pressure system capable of circulating water at about 8 lpm and ~10psi. It offers a significant advantage over a positive pressure solution, as if there is a leak in the system, it will draw air into the tube instead of letting water out and potentially damaging electrical components. The disadvantage being that the water in the line would be replaced by air, reducing the cooling efficiency. This can be monitored and controlled to some degree with the distribution panel. The panel will also allow for the parallel loops of the on-detector cooling system to be monitored and adjusted, should any of the loops get hotter than the others or similar circumstances of unbalance.

The on-detector part of the cooling system (titanium pipes, aluminum cold plates and water) were implemented in the GEANT model as shown in Fig. 2.7 to account for their contribution to the overall material budget in the acceptance of the ePIC backward crystal electromagnetic calorimeter.

2.7 Gas system

The proposed gas system for the pfRICH detector will supply pure, industrial grade nitrogen from a cryogenic liquid cylinder. An online compressed gas cylinder will provide a backup

in the case of an unforeseen emergency. A schematic diagram of the system can be found in Fig. 2.8. A 0.5μ filter and silica gel dryer will be added to the input line to filter dust particles and dry the gas, respectively. Gas to the pfRICH vessel will be delivered at a few millibars above the atmospheric pressure using an industrial tank blanketing pressure regulator (TBPR). The TBPR ensures that the pressure inside the chamber is kept at a given value slightly above atmospheric pressure regardless of atmospheric pressure changes, which will prevent air from the environment from entering the vessel. An over pressure protecting bubbler will provide secondary protection in any unforeseen events. All the used gases will be vented outside the experimental hall. Pressure gauges and pressure transmitters will be placed in various locations in the gas system to monitor and archive the pressure readings. A flowmeter will be added to control the flow of nitrogen through the detector. The nitrogen flow rate is envisioned to be a couple of volume exchanges per hour, and the exact rate will be finalized at a later stage.

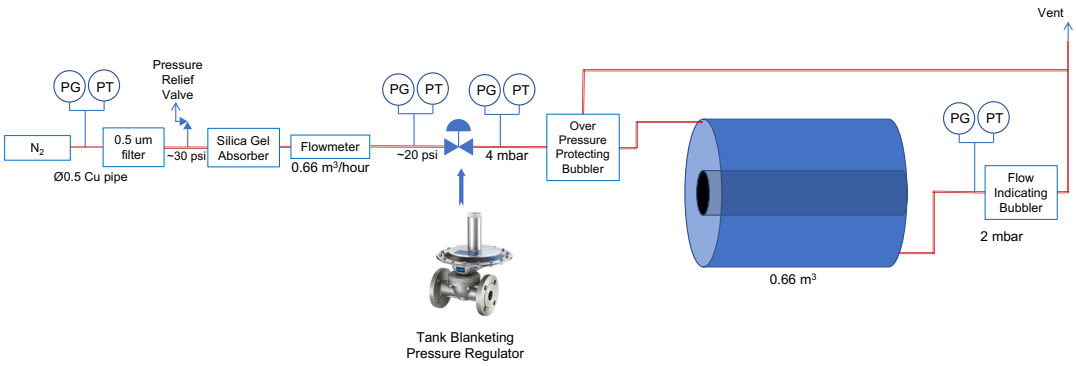

Figure 2.8: Schematic of the proposed gas system.

Chapter 3

Machine environment

3.1 HRPPD in magnetic field

The performance of the photon sensors may be significantly affected when exposed to a high magnetic field, especially when oriented at angles not perpendicular to the sensor plane. Tests on an HRPPD prototype in a high magnetic field, oriented at non-zero angles with respect to the sensor, were recently (February 2023) carried out at Argonne National Laboratory with field strengths and orientations based on what can be expected in ePIC at the location of the pfRICH. Figure 3.1 (left) shows the longitudinal component of the ePIC solenoid magnetic field map. In extreme cases, the sensor is exposed to a magnetic field of 1.38 Tesla oriented at an angle of 12.6 degrees.

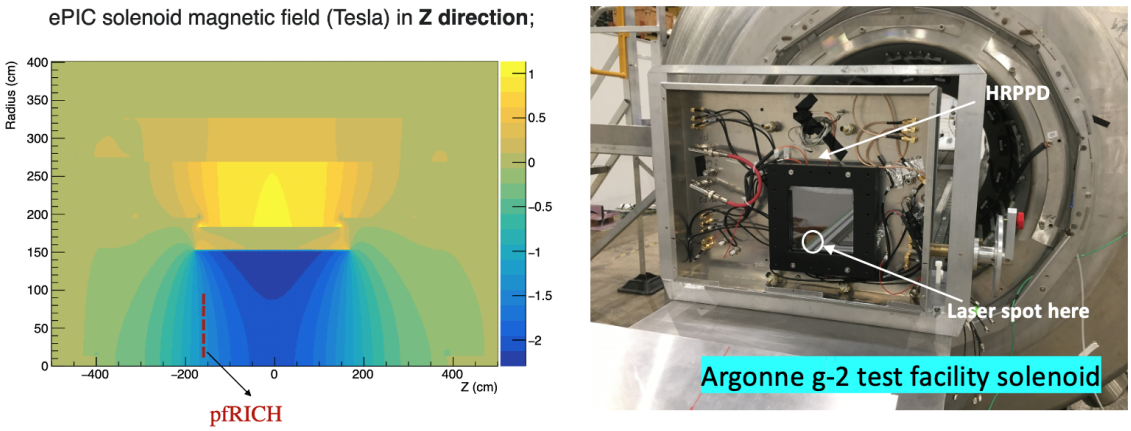

Figure 3.1: ePIC solenoid magnetic field in the beam direction (left) and HRPPD installaed in a black box, ready to be moved into a large bore solenoid (right).

Tests of the HRPPD prototype at Argonne National Laboratory were carried out using the superconducting magnet from a decommissioned MRI scanner, see Fig. 3.1 (right). This magnet provides a large bore, with a diameter of 68 cm, a very homogeneous field (7 ppb/cm), and a tunable field strength of up to 4 T. Measurements were performed by Argonne and Incom personnel, with guidance and data analysis provided by eRD110

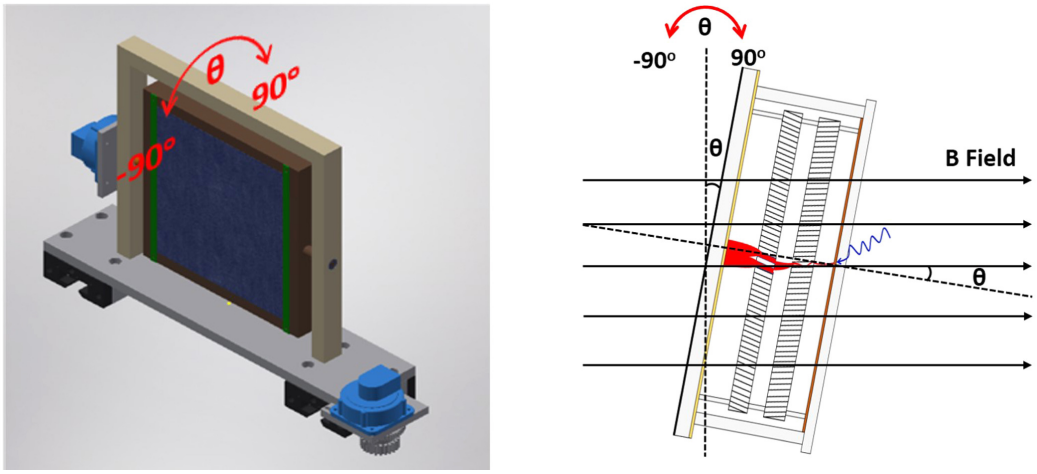

Figure 3.2: (left) AutoCAD drawing of the custom designed magnetic field tolerance test platform. The central part is rotatable with an angle $\theta(-90° \leq \theta \leq 90°)$. (right) Schematic of the setup of the HRPPD rotated by an angle θ relative to the magnetic field direction.

pfRICH members. A characterization system compatible with the solenoid magnet was assembled to test the performance of the HRPPD prototype.

A non-magnetic, light-tight dark box was built to contain the HRPPD prototype during testing, and the dark box was held on a platform with the detector surface normal to the direction of the magnetic field. The position of the dark box was adjusted so that the center of the HHRPPD photon sensor was aligned with the center of the solenoid magnet. A rotation mechanism was integrated into the system, able to rotate the HRPPD prototype by an angle $\theta(-90° \leq \theta \leq 90°)$, as illustrated in Fig. 3.2. A PiLas040XMS laser system provided the light source, and the light was guided into the dark box via an optical fiber. High voltage was applied to the HRPPD prototype from a power supply with continuous voltage control. Signals collected at the striplines were read out through a DT5742 desktop digitizer with a sampling rate of 5 GS/s, produced by CAEN.

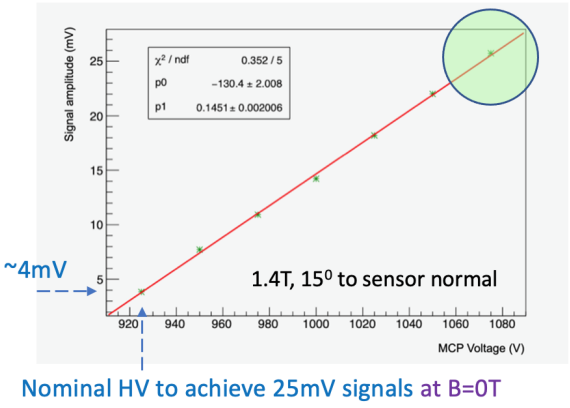

Figure 3.3: By increasing the MCP voltage from its nominal setting of 925 V at B=0T to 1075 V it is possible to restore signal amplitude of 25 mV corresponding to the B=0T field case.

First results from these tests look very encouraging. It appears possible to fully restore the HRPPD gain at a field of 1.4 T and angle up to 15 degrees by increasing the MCP voltage by only $\sim 150\ V$, see Fig. 3.3.

3.2 Particle Occupancy

Because the pfRICH covers a negative pseudorapidity region, opposite the direction of the hadron beam, the overall particle momenta and multiplicities in the detector will be small. While the average particle load incident on the pfRICH will be low, there will be areas of phase space, mostly at large inelasticity (y) values, with much higher hadronic activity at negative pseudorapidity. It is important to quantify particle multiplicities in these high occupancy regions of phase space to understand any potential degradation in PID capability due to particles in close proximity to one another.

The multiplicity results presented below were carried out at particle level (no detector response was simulated) using a dedicated ep PYTHIA-6 Monte Carlo sample spanning a Q^2 range of 10^{-5} to 10^3 GeV^2. This sample was used in place of the official ePIC simulation to ensure sufficient statistics at all Q^2 values, especially below 1 GeV^2. PYTHIA-6 was chosen as the event generator as opposed to the more modern PYTHIA-8 due to the later having known issues simulating the Q^2 range between roughly 10^{-1} and 10 GeV^2. To ensure the validity of the particle level sample, a dedicated comparison with the official ePIC detector level simulation was performed over a narrow Q^2 range ($1 < Q^2 < 10$ GeV^2) where sufficient statistics exist and the results were found to be nearly identical.

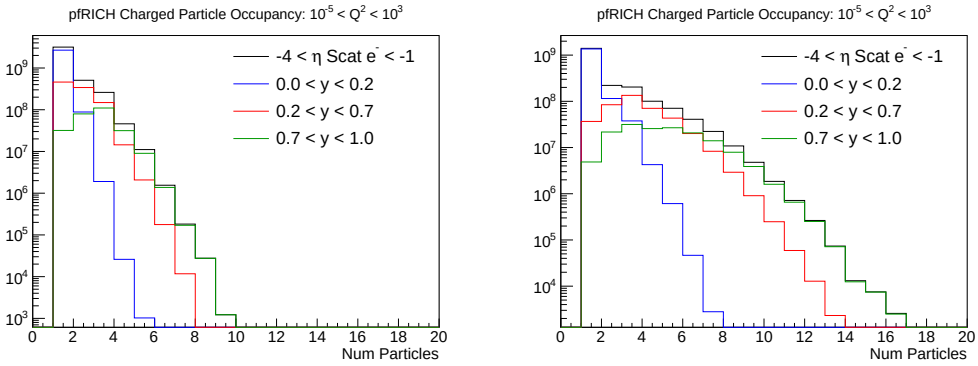

Figure 3.4: Expected number of events containing a given number of charged particles within the approximate pfRICH acceptance $-4 < \eta < -1$ for all events (blue curve) and events with the scattered electron in the acceptance (red curve) for 5x41 GeV (left) and 18x275 GeV (right) beam energies.

The charged particle multiplicity in the approximate pfRICH acceptance ($-4 < \eta < -1$) and different inelasticity bins for beam energy combinations of 5x41 GeV and 18x275 GeV for the case when the scattered beam electron is in the acceptance are presented in Fig. 3.4. The curves have been scaled to 1 fb^{-1} and thus can be interpreted as the number of events containing a given number of charged particles per femtobarn of integrated luminosity. The majority of events have inelasticities less than 0.2 and low charged particle multiplicities in the pfRICH acceptance, while higher multiplicity configurations are dominated by events with larger inelasticity. This is also seen in Fig. 3.5, which shows the $x - Q^2$ distribution of events with different pfRICH multiplicities for the 18x275 GeV beam energy configuration.

Along with knowledge of the typical number of particles in the pfRICH, it will also be important to quantify the physical spacing between particles in order to better un-

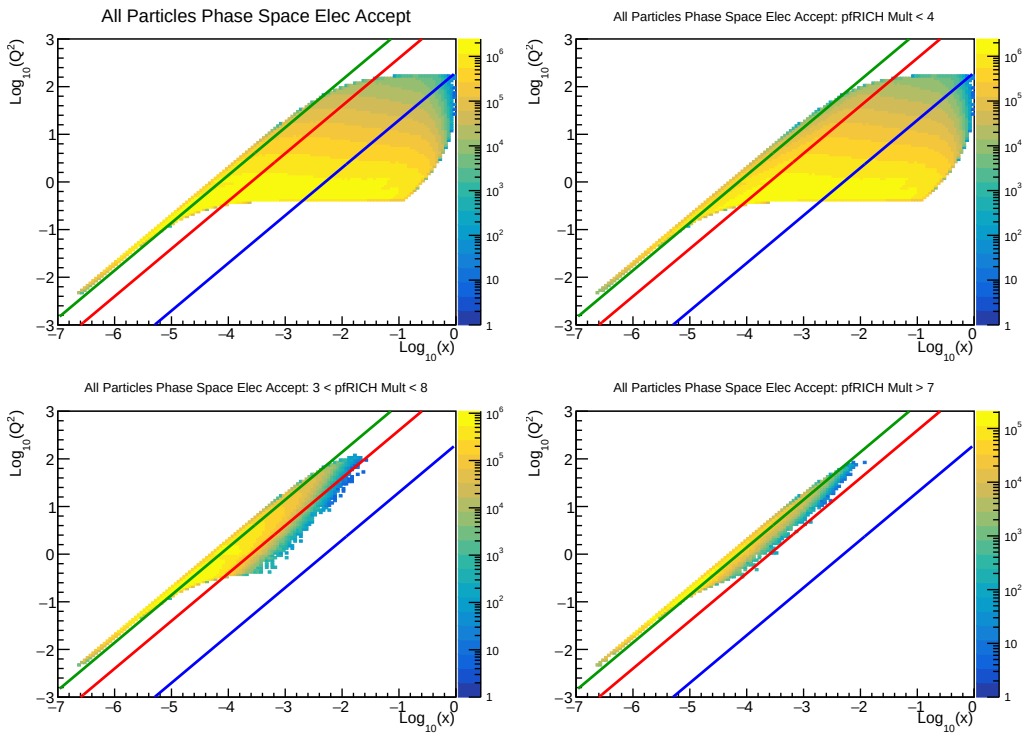

Figure 3.5: Q^2 versus x distribution of events with the scattered electron in the approximate pfRICH acceptance ($-4 < \eta < -1$) for the 18x275 GeV beam energy configuration. The panels display the $x - Q^2$ distribution for different multiplicities of charged particles in the acceptance region. Clockwise from top left: all events, multiplicity ≤ 3, multiplicity ≥ 8, and $4 \leq$ multiplicity ≤ 7. The blue, red, and green lines show constant inelasticity values of 0.01, 0.2, and 0.7, respectively.

derstand possible impacts on PID efficiency due to interference between nearby particles. The distance between charged particles was found by projecting the (straight-line) particle trajectory onto a plane perpendicular to the electron beam line at a $z-$position of -1570 mm, the approximate position of the pfRICH sensor plane. For events with more than one charged particle in the range $-4 < \eta < -1$, the pair whose intersections with the plane are closest in space are found. The distribution of $x - y$ distances between the closest particles in an event are shown in Figs. 3.6 and 3.7 for all events and those events in which the electron is in the pfRICH acceptance, respectively. Distances are presented for the 5x41 GeV and 18x275 GeV beam energy configurations as well as for three bins in inelasticity, corresponding to the low, medium, and high occupancy regions. As expected, high-y, high multiplicity events have the smallest minimum distances between particle pairs with the most-probable distances increasing for lower inelasticity. It is seen that the most-probable minimum separation is smaller for higher beam energies and for events in which the electron is in the pfRICH acceptance.

In addition to providing hadron PID capabilities, the pfRICH will be able to discriminate between hadrons and electrons and thus aid in the identification of the scattered beam

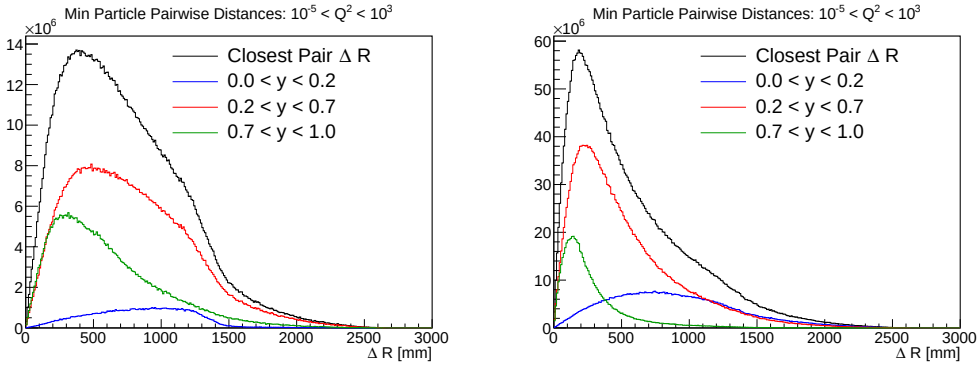

Figure 3.6: Distance between closest pair of charged particles in the approximate pfRICH acceptance at the depth of the sensor plane for different bins of inelasticity for the 5x41 GeV (left) and 18x275 GeV (right) beam energy configurations. All events are included.

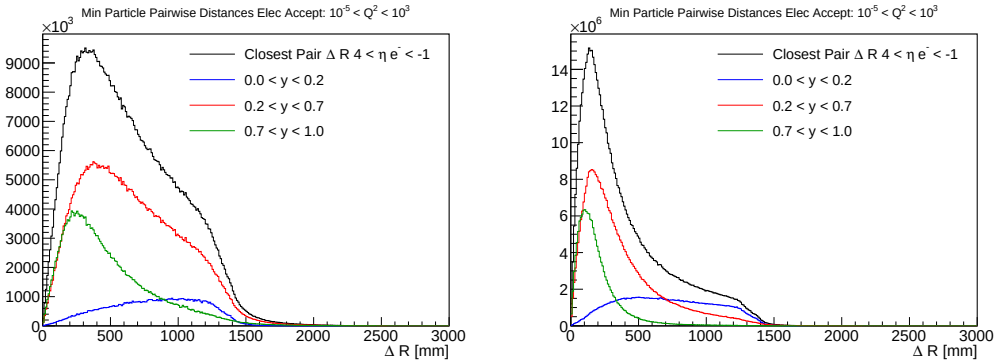

Figure 3.7: Same as Fig. 3.6 but requiring that the scattered electron is within the approximate pfRICH acceptance ($-4 < \eta < -1$).

electron, which will be crucial to determining the event kinematics in the critical Q^2 region of roughly 10^{-2} to 10 GeV^2. Because the identification of electrons will play such an important role in nearly every ePIC analysis, special attention should be paid to potential contamination from other nearby particles which may degrade electron-hadron discrimination capability. The fluxes of particles in close proximity to the scattered electron are quantified in Fig. 3.8, which show the fraction of events which contain a given number of charged particles within 20 cm of the scattered electron, which is a little wider than the expected extent of the Cherenkov ring. The results are again shown for the 5x41 GeV and 18x275 GeV beam energy configurations and different inelasticity bins. The area of each inelasticity curve has been separately normalized to unity so they can be interpreted as the fraction of events in that particular inelasticity range containing a given number of particles in proximity to the electron. For example, the green curve in the right panel of Fig. 3.8 indicates that roughly 55% of events with inelasticities greater than 0.7 will have no charged particles, 30% will have one charged particle, and 10% will have two charged particles within 20 cm of the scattered electron. As expected, these distributions follow

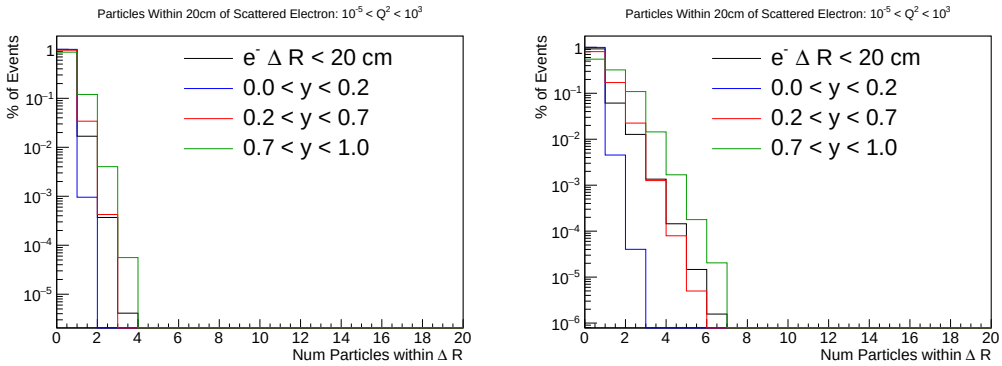

Figure 3.8: Percentage of all events, and events in different inelasticity bins that contain the indicated number of charged particles within 20 cm of the scattered beam electron for the 5x41 GeV (left) and 18x275 GeV (right) beam configurations. The full event sample (black) and each inelasticity bin sample are all normalized separately to unity.

the same trends as the minimum distance curves in Figs. 3.6 and 3.7 with the frequency of particles in proximity to the electron increasing with beam energy and inelasticity.

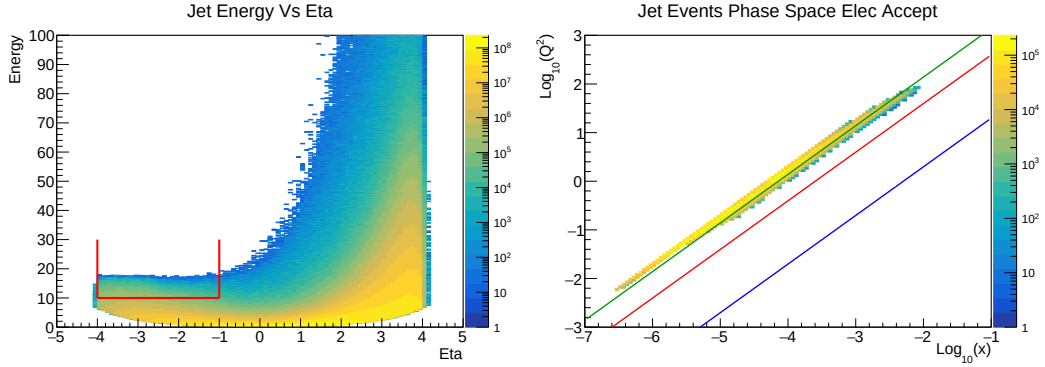

Figure 3.9: (Left) Jet energy versus pseudorapidity for the 18x275 GeV beam configuration. The red lines denote the jets selected for this analysis. (Right) Q^2 versus x distribution of events with a jet in the phase space region defined in the left panel and the scattered beam electron in the approximate pfRICH acceptance. The blue, red, and green lines show constant inelasticity values of 0.01, 0.2, and 0.7, respectively.

One observable that may be particularly affected by high particle occupancy rates in the pfRICH are jets, which by definition consist of a number of particles in relatively close proximity. As can be seen in the left panel of Fig. 3.9, the number of jets in the backward region with reasonably high energies constitute a small fraction of the overall number of expected jets throughout the full experimental phase space. However, because of the high expected luminosities at the EIC, there will still be a large absolute number of jets in this region, justifying studies of the properties of jets in the pfRICH. For these studies, jets were clustered from all stable particles using the Anti-k$_T$ algorithm with a recombination parameter, R, of 1.0. Jets were required to have transverse momentum greater than 1 GeV,

but total energy of greater than 10 GeV, and a thrust axis restricted to $-4 < \eta < -1$. Note that only results from the 18x275 GeV beam energy configuration are shown, as jets from the 5x41 GeV configuration do not reach the 10 GeV energy cutoff.

The jets considered here come from the highest inelasticity region of the event phase space as shown in the right panel of Fig. 3.9. This is the region with the highest charged particle multiplicities in the pfRICH acceptance and also corresponds to the region in which the struck parton follows the direction of the outgoing electron beam. The majority of jets which have a thrust axis between -4 and -1 in pseudorapidity contain one charged particle in that same acceptance and the probability that the jet contains a larger number of charged particles decreases somewhat more rapidly than the overall charged particle occupancy curve for the range $0.2 < y < 0.7$ shown in Fig. 3.4. The distances between the closest pair of charged particles within a jet in the pfRICH acceptance are also compared with the distances in the entire pfRICH for the $0.2 < y < 0.7$ and $0.7 < y < 1.0$ bins as shown in Fig. 3.6 and 3.7. For all events, the jet distance distribution seems to lay somewhat between the medium and high inelasticity bins, while for the case where the scattered electron is in the pfRICH acceptance, the jet curve follows very closely the medium inelasticity curve. Both cases show that the typical minimum distance between particles inside a jet is not significantly different than for the entire pfRICH for inelasticity values greater than 0.2.

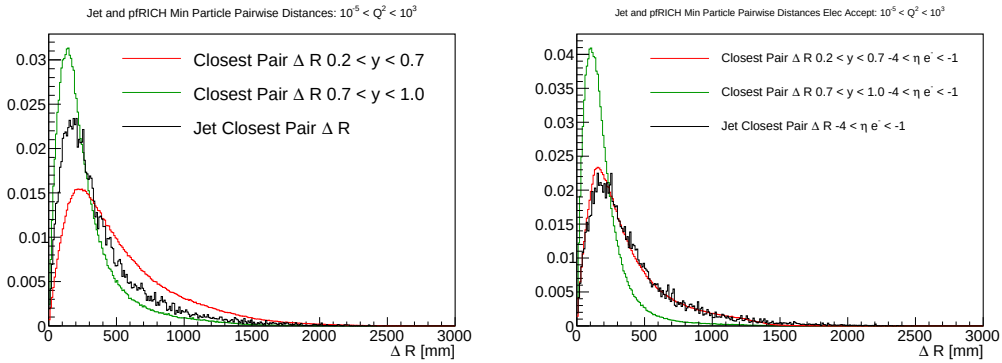

Figure 3.10: Comparison of the distance between the closest pair of charged particles in the approximate pfRICH acceptance ($-4 < \eta < -1$) for the $0.2 < y < 0.7$ and $0.7 < y < 1.0$ bins and the closest pair of charged particles within a jet for the 18x275 GeV beam configuration for all events (left) and events where the scattered electron is within the pfRICH acceptance (right). All curves have been normalized to unity to facilitate shape comparisons.

Chapter 4

Detector Performance

4.1 Simulation and reconstruction framework

A custom software suite [19] was written from scratch to conduct the detector simulations. Besides GEANT4 v10.05.p01 [20] and ROOT v6.18.04 [21] the software made use of the Inverse Ray Tracing (IRT) library, which is part of the ePIC software stack [22].

4.1.1 Geometry description

The geometry description implemented in GEANT was made as realistic as possible. The model includes the following considerations:

- The pfRICH location and boundary conditions in ePIC were observed carefully when deciding on the layout of the detector, and absence of conflicts with the surrounding equipment was cross-checked using both CAD and GEANT models, which were identical in all essential parts.
- The vessel walls (a honeycomb carbon fiber sandwich with reinforcement elements at the edges) were modeled according to the existing implementation of the sPHENIX TPC vessel [3], with an overall core thickness of 1/2" (outer wall) and 1/4" (inner wall and front plate). However, aluminum as a reinforcement material was replaced by PEEK in order to reduce the material budget while retaining required structural strength.
- The conical mirrors were modeled, according to feedback from the manufacturer Composite Mirror Applications (CMA) [23], as a 1 mm thick carbon fiber piece for the inner mirror, and 2 mm thick cone for the outer one.
- The aerogel container was modeled as a carbon fiber matrix with 500 um separator walls.
- Individual HRPPD "windows" in the 1/2" thick aluminum mounting plate were described as a 1:1 copy of the CAD model.

- The HRPPD sensor description included all of the structural components (window, side walls, MCPs, base plate, readout PCB), with a sensitive volume (bialkali) placed right behind the quartz window.
- Cooling system elements (1/4" pipes, water volume, cold plates) were modeled according to the description given in section 2.6.

A material scan of the beam pipe area is shown in Fig. 4.1. Our studies show that this amount of material has minimal impact on the backward EmCal performance, see Fig. 7.4.

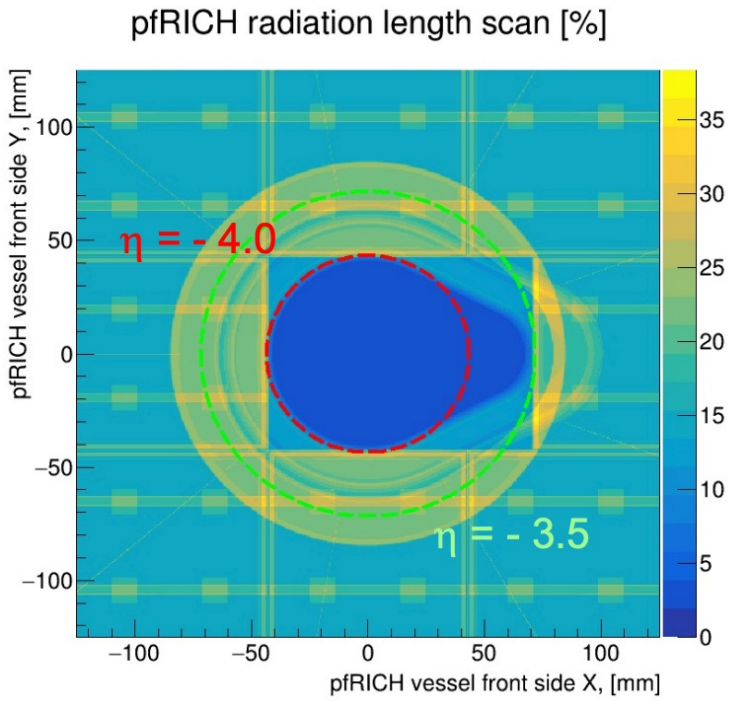

Figure 4.1: pfRICH detector material scan in the area around the beam pipe. HRPPD sensor boundaries, cooling system pipes and cold plates, as well as the inner vessel wall and the inner conical mirror can be clearly seen.

4.1.2 Simulation

- The ePIC solenoid magnetic field map at 2.0 T was used in the simulations [24].
- Optical media involved in the simulation (aerogel [25], acrylic filter [26], nitrogen [27], quartz [28]) were described precisely, to the best of our present knowledge, including wavelength dependencies of the refractive index, absorption length and Rayleigh scattering length. Aerogel RAYLEIGH / ABSLENGTH / RINDEX parameterizations are shown in Fig. 4.2.

- The HRPPD QE curve presented at [8] was taken as a reference (see Fig. 4.3), but renormalized for a peak value of 30% times a safety factor of 0.7, accounting for unexpected imperfections in the real life experimental setup as compared to the idealized Monte-Carlo simulation.

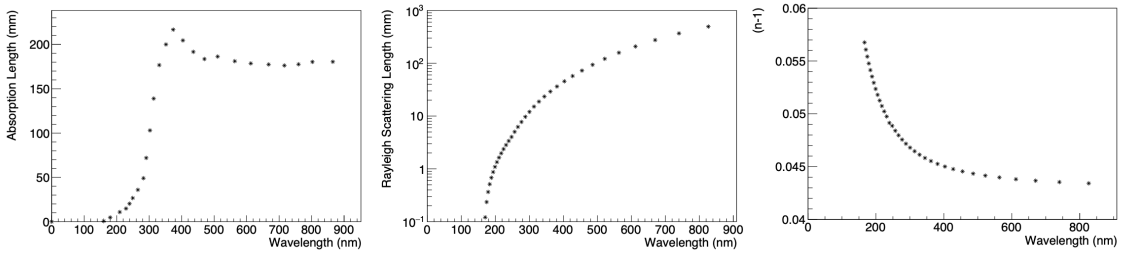

Figure 4.2: Belle II aerogel#1 (n = 1.045) optical properties used in the GEANT simulations.

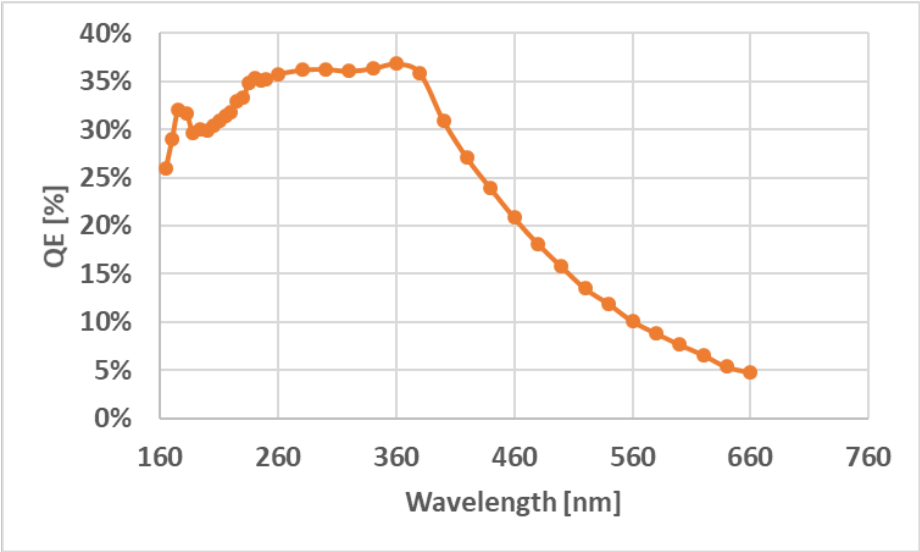

Figure 4.3: LAPPD tile #126 QE spectrum.

4.1.3 On-the-fly calibration

With a lack of tracking tools, as well as the optical system calibration files that typically become available several months after the experiment start-up (like parameterizations of the single photon Cherenkov angular resolution as a function of primary particle incident angle), Cherenkov photons produced in all optical media (aerogel, acrylic filter, gas, quartz) that reached the photocathode but were not counted as "detected" because they did not pass the QE test, were utilized. The location of these photons along the charged particle trajectory was used as an imitation of an ideal tracker. The GEANT global time at the vertex was used to evaluate the charged particle trajectory length. These "calibration photons"

were also accounted for in the calculation of the emission point depth in the aerogel radiator, effectively taking into account photon losses because of absorption and Rayleigh scattering.

4.1.4 Digitization

Photons entering the photocathode physical volume inside a particular HRPPD were accounted for in such a way that a single digitized hit was produced per pixel that was hit, independently of how many photons were detected at this location. The hit coordinate was taken to be the center of the pixel. It was assumed that performing an imaginary pixelation of the photocathode layer is sufficient to describe the position of the electron avalanche if it was properly propagated through the MCP stack. The latter option was discarded for practical reasons, as it would require an enormous amount of computing power, while not necessarily providing a better description of the real setup. Using the "calibration photon" sample (see Sec. 4.1.3), digitization procedure provided the means to automatically exclude the sensor pad areas from imaging, which would be dominated by Cherenkov photons produced either in gas or in HRPPD windows.

4.1.5 Reconstruction

A custom software framework independent, fully deterministic event-level ring imaging reconstruction algorithm was implemented for reconstruction. At its core, it is based on a χ^2 statistical analysis of hit-to-track assignment, ambiguity resolution, and overall goodness of fit evaluation for complete events. Cumulative χ^2 distributions are verified at every step (hits, tracks, event), namely it is cross-checked that they follow the tabulated ones for a given number of degrees of freedom, provided the detector resolution input (SPE Cherenkov angle resolution and timing resolution) is incorporated correctly. Single photon and track-level Cherenkov angle residual plots are readily available at the end of the event reconstruction procedure. We believe that (despite the apparent combinatorial overhead) in this early stage of the project such an event reconstruction paradigm is superior to either extended maximum likelihood (ML) or Artificial Intelligence / Machine Learning (AI/ML) techniques, which tend to obscure the essential details of the reconstruction process important for geometry optimization by a human being. It is expected though that with time either one of these techniques will take over, also because of the CPU efficiency considerations, and the algorithmic scheme presented here will be used only as a legacy tool for validation purposes.

The utilized code does not have a configuration database, an ASCII configuration file parser, or a fixed data model. All of the essential parameters are hard-coded as #define statements in a pair of C++ include files (a lengthy "fixed" one with all of the agreed upon geometry definitions, and a very short one for tuning purposes). The data model is replaced by a persistency scheme making full usage of ROOT serializer capabilities. Similar to the FairRoot [29] and fun4all [30] frameworks, a C++ class instance representing a single Monte-Carlo event after the GEANT transport pass is written in its entirety into a ROOT tree and saved to disk. Later on, these events are retrieved in the reconstruction code with all their initial non-trivial STL library based connections between classes representing geometry, particle tracks, and optical photons. We believe this scheme is particularly useful in the early stage of the detector design optimization, where fine details of the data model

in the reconstruction code may change often, with new fields in the data structures re-added frequently (and often deleted shortly afterwards). In general, it may be more convenient to have all of the essential parameters available in one place, rather than distributed all over the code base with convoluted parsers involved.

The event record after the GEANT pass has a full snapshot of optical photon kinematics, emission vertices, (optionally) all reflection and refraction points, as well as detection points in their respective HRPPD photocathode volumes. This same event record is imported back from a ROOT tree, appended with the respective (non-persistent) C++ class instances during the reconstruction stage, and all information at once is available to the end user in their ROOT macro via respective methods and/or plain structure fields for a detailed analysis.

It is worth mentioning that the developed reconstruction procedure must be equally applicable to the optimization and performance evaluation of the ePIC dual-radiator RICH detector (dRICH), including its possible more advanced configurations (reflecting mirrors around the beam pipe area, dual-mirror configuration, etc). The codes are readily available in the ePIC software repository.

At the moment, the scope of this code is limited to ring imaging for photons originating from the aerogel radiator. A step-by-step description of the algorithmic part follows.

PID hypothesis choice

The user has an option to declare which particle mass hypotheses are of interest in their ROOT macro used during the reconstruction phase. Two typical choices are (1) electron and pion, (2) pion, kaon and proton. The algorithm will then only consider these particular hypotheses for further evaluation of events in a given Monte-Carlo input file.

Track parameterization

Charged particle trajectory parameters at the pfRICH aerogel location (momentum, impact point, and angles) are assumed to be known well enough for the purposes of ring finding. Recently (March 2023) tracking resolution parameterizations were incorporated in the pfRICH reconstruction code, but they are not yet used to resolve hit-to-track assignments. In other words, the procedure derives the track parameters from the collection of 3D vertices of the otherwise unused abundant "calibration photons" (see Sec. 4.1.3), which is a minor simplification in particular for high momentum tracks where the ePIC tracker provides angular resolutions well below 1 mrad (compared to the pfRICH SPE Cherenkov photon resolution of $\sim$4.5 mrad).

Digitized hit pre-selection

As mentioned earlier, the SPE Cherenkov angle resolution for a track with a given η is evaluated using "calibration photons" in the first few hundred events of the input MC file. An IRT pass is then run on all [hit,track] pairs of a given event, for all defined optical path configurations (to first order, those are a direct path between the evaluated emission point and the detection point and a path including a reflection on one of the conical mirrors).

Only those digitized hits that are consistent (within a configurable +/- Nσ band) with at least one PID hypothesis of at least one charged particle track, are retained for further processing. Photon arrival time at the photosensor can optionally be accounted for in this procedure as well, mainly as a means of ambiguity resolution between direct and reflected photon paths, where the full path length can be different by several centimeters between these two cases.

An overwhelming majority of the Rayleigh scattered stray background photons get rejected at this stage. It is worth mentioning that Dark Count Rate signals in the HRPPDs will barely contribute to the "background hit" sample either, because at their expected rate of ~ 1 kHz/cm^2 they will be suppressed to almost a negligible contribution by a timing cut, even for a generously chosen timing acceptance window as wide as 1 nsec.

Combinatorial χ^2 evaluation

Given M particle hypotheses, an event with N tracks will have N^M possible PID combinations to consider. They are all evaluated one by one, with each hit being either assigned to one (and only one) [track, hypothesis] pair that provides the smallest 1D $\chi^2 = (\theta - \theta_0)^2/\sigma^2_{SPE}$, or retained as a "background" one, if none of the evaluated 1D χ^2 estimates falls within a specified +/- Nσ window. In the above formula θ is the measured Cherenkov angle for a given [hit, track] combination, θ_0 is the expected Cherenkov angle for a given particle 3D momentum and mass, and σ_{SPE} is a single photon Cherenkov angle resolution. Once all hits are unambiguously associated with their respective tracks, the track-level and event-level χ^2 estimates are simply a sum of 1D χ^2's over respective hits.

A combination of particle hypotheses with the smallest event-level χ^2 is the output of the reconstruction procedure. It is expected that (1) for a correctly resolved PID assignment, the respective event-level χ^2 should follow the tabulated one for a given number of degrees of freedom, (2) all other $[N^M - 1]$ "wrong" combinations will have their χ^2 estimates towards the tail of the tabulated χ^2 distribution, and manifest themselves as a sharp peak around zero in a cumulative χ^2 distribution plot. By examining this plot one can define which events have PID assignments more reliable than others, and apply efficiency cuts on event-by-event basis in the subsequent analysis.

Poissonian terms in the χ^2 evaluator

Since the expected number of emitted (and detected) Cherenkov photons is proportional to $sin^2(\theta)$, from first principles, it was worth adding a respective Poissonian term to the χ^2 evaluation ansatz, following the prescription given in [31], although the effect of its incorporation has not yet been studied in detail. In the future, one should also add a similar penalty term to account for the remaining "background" hits, which happened to be consistent with at least one [track, hypothesis] pair after the hit pre-selection stage, but were not assigned to any track for a given PID hypothesis combination.

4.2 pfRICH performance and validation

Thorough pfRICH performance studies have been carried out for the validation of our detector geometry and software. These studies used both single particle events generated using a particle gun to study the consistency of the simulation data as well as multiple particle events to test the robustness of the reconstruction algorithm.

4.2.1 Consistency checks using event display

The first step of the simulation evaluation was to verify the geometric features from the event display and to validate the reconstruction algorithm in extreme cases. Particles entering the pfRICH at extreme angles generate photons that will be reflected back by the outer mirror, substantially distorting the resulting ring shape (see Figs. 4.4a and 4.4c for comparison). Despite this difficulty, the reconstruction algorithm was able to accurately reconstruct the ring angle. This algorithm uses an inverse ray tracing method [22], which is able to handle both direct and reflected photons, and compute single photon Cherenkov angles from the detected position of a single photo-electron (SPE). These simulation studies have also demonstrated that the reconstruction algorithm produces a consistent Cherenkov angle estimate independent of the primary charged particle pseudorapidity (see figure 4.4b and 4.4d for comparison). A substantial variation in SPE Cherenkov angle resolution, clearly seen in Fig. 4.5 (left), is caused by the fact that at large polar scattering angles of a primary charged particle, the emission point uncertainty strongly depends on whether a photon was emitted in the direction of the beam pipe or towards the outer circumference of the detector.

4.2.2 Number of detected photons

First principles estimations indicate that a saturated particle should produce roughly 11-12 detected photo-electrons. This number takes into account a realistic sensor surface quantum efficiency, as measured by Incom [8], and a conservative safety factor of 0.7. In figure 4.6a, it is seen that the mean of the Possionian is around 11.6, which is in good agreement with the expectation. In the same figure, a spike for track with no detected photons can be seen. This effect becomes important when near the geometric boundary.

The simulation showed that for saturated pions, the number of detected photo-electrons drops sharply for particles impinging on the aerogel with pseudorapidity above -1.5 and below -3.5, providing a hint of the working acceptance limits. The simulation accounts for a finite primary vertex distribution width of $\sigma \sim 10$ cm along the beam line at the IP, meaning the acceptance for charged particles will be smeared around the otherwise sharp boundaries. There is also a loss of photons due to a blind spot on the inner mirror. In order to estimate an average working acceptance, the acceptance for saturated particles is defined using the following equation:

$$\text{acceptance} = \frac{N_{\text{track}}(N_{pe}) > 0}{N_{\text{track}}}, \tag{4.1}$$

where N_{track} is the total number of tracks and $N_{\text{track}}(N_{pe}) > 0$ is the number of tracks with at least one produced photon. We have assumed that the Poisson probability to obtain

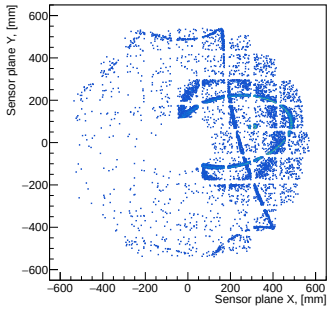

(a) Photons reflected from the mirror detected in the sensor plane. As viewed in the event display

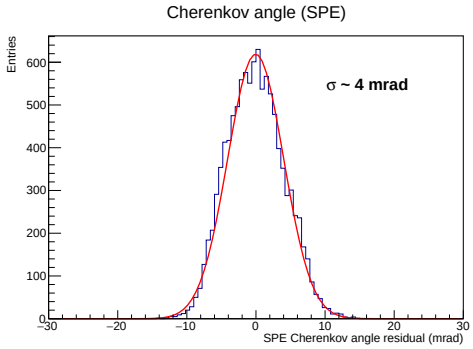

(b) Reconstructed SPE Cherenkov angle

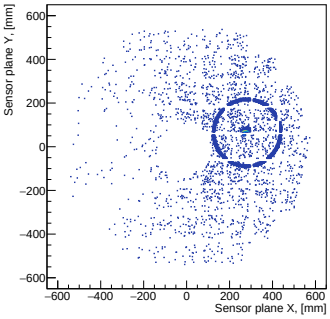

(c) Photons coming directly from the aerogel detected in the sensor plane. As viewed in the event display

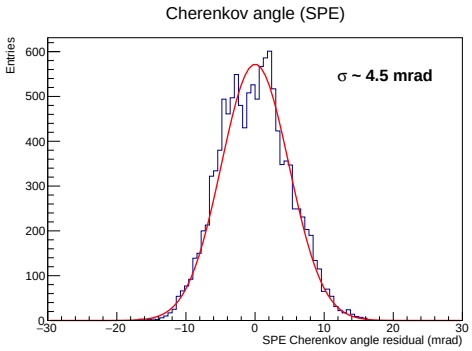

(d) Reconstructed SPE Cherenkov angle

Figure 4.4: Event display of detected photons (left panels) and the reconstructed Cherenkov angle (right panels) for a particle with $\eta = -1.5$ (top panels) and $\eta = -2.5$ (bottom panels).

zero photons from a distribution with a mean of 11 is negligible. Figure 4.6b presents the acceptance as a function of pseudorapdity and it is seen that the pfRICH can comfortably cover the region $-3.5 < \eta < -1.5$. Apart from the edge rapidity (-3.5 and -1.5) a constant acceptance greater than 95% is achievable. Whereas, around the border region, the acceptance drops sharply.

4.2.3 Angular Resolution

Both the track level (σ_{Ch}) and single photo-electron (σ_{SPE}) resolutions were extracted from the simulation. Over the momentum range and particle pseudorapidity relevant for the pfRICH, σ_{SPE} remains overall constant, which is consistent with expectations. However, photons coming from tracks entering at an angle close to the outer mirror are better resolved due the effect of the reflection. The SPE resolution between pseudorapidities of -3.5 and -1.5 is around 4.75 mrad (Fig. 4.7a). The track level angular resolution (Fig. 4.7c) however, scales with the number of detected photons (Fig. 4.7b). Full consistency between the track

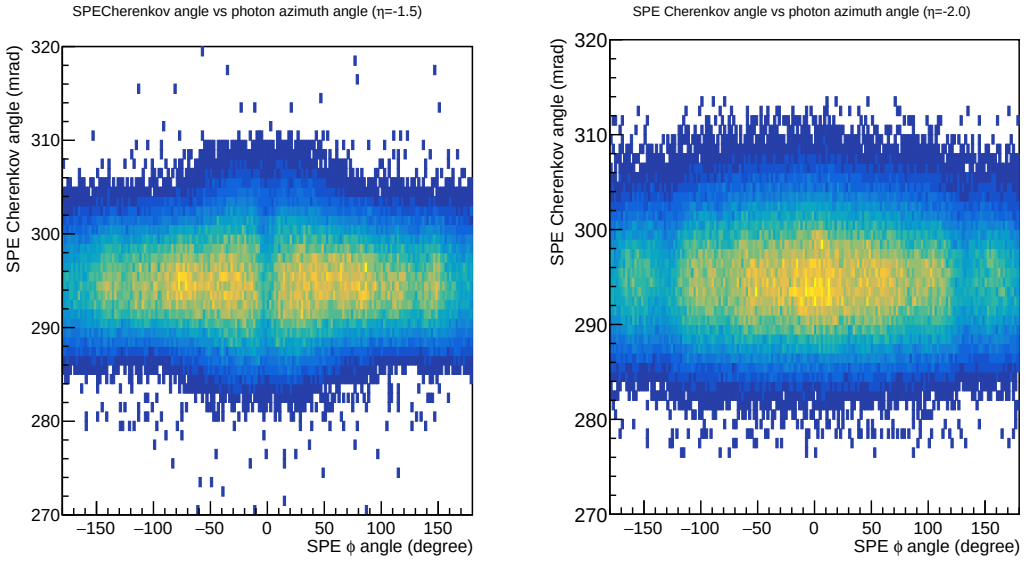

Figure 4.5: Dependence of SPE Cherenkov angle with SPE azimuth angle at different pseudoradpity. Left panel: η=-1.5, right panel: η=-2.0

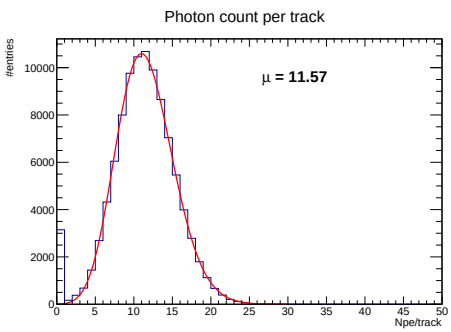

(a) Number of photons detected for 7 GeV/c pion at -2.0 pseudorapidity

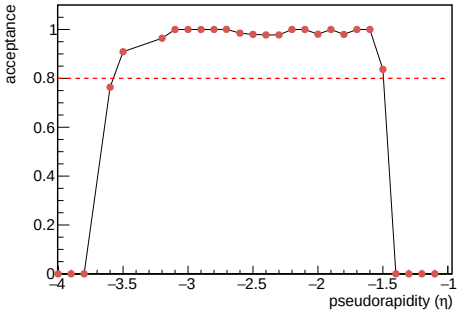

(b) pfRICH acceptance as a function of pseudo-rapidity. Apart from the acceptance boundary areas, a constant value greater than 95% is achieved.

Figure 4.6: Number of photons and acceptance

level ring resolution, SPE resolution and the number of detected photons is observed.

4.2.4 Reconstructed Cherenkov angle

The algorithm for event based reconstruction of the Cherenkov angles was validated using multi-particle simulations. The reconstructed Cherenkov angle (in units of mrad) as a function of particle momentum (in units of GeV/c) is shown in Fig. 4.8a and compared to the theoretical expectations for a given mass hypothesis. It is seen that the reconstructed

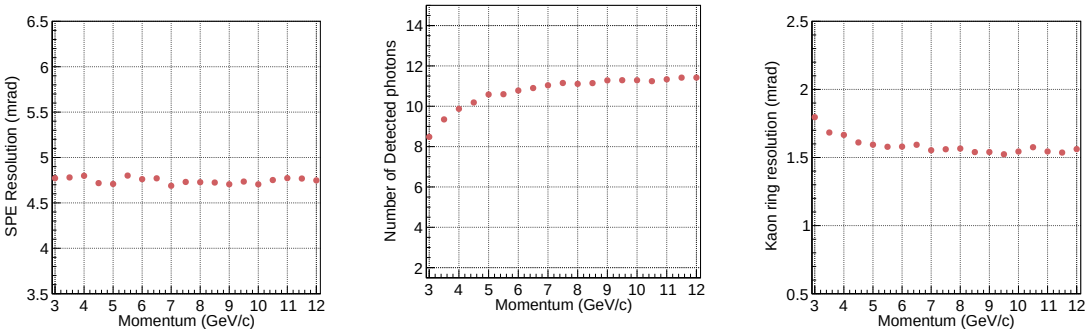

(a) SPE resolution is constant over momentum for kaon samples

(b) Momentum dependence of the detected number of photo-electrons for kaons.

(c) Evolution of kaon ring resolution with momentum.

Figure 4.7: Single photo electron resolutions, number of detected photons and ring resolutions for kaon samples

angles and theoretical expectations are in good agreement, confirming that the event based reconstruction is performing well. This plot also shows that the Cherenkov saturation angle is approximately 295 mrad and that 3σ electron-pion separation can be expected up to a momentum of 3 GeV/c, while 3σ pion-kaon separation can extend to a momentum of 9 GeV/c. These distributions can be linearized by plotting the square of the Cherenkov angle as a function of the inverse squared momentum as in Fig. 4.8b. The slope values of the linear distributions are dictated by the particle squared masses and the intercepts are dictated by the squared Cherenkov saturation angle, that is $2(n-1)$, where n is the refractive index of the medium.

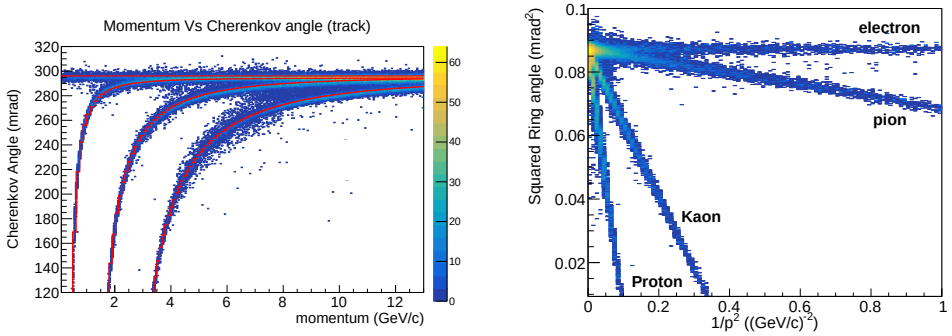

(a) Reconstructed Cherenkov angle for particles as a function of particle momentum

(b) Reconstructed squared Cherenkov angle for particles as a function of inverse squared momentum

Figure 4.8: Reconstructed Cherenkov angle

$$\cos\theta = \frac{1}{n\beta}$$
$$\theta^2 \sim 2(n-1) - \frac{m^2}{p^2} \tag{4.2}$$
$$\theta^2 \sim \theta^2_{\text{sat}} - \frac{m^2}{p^2}$$

Equation 4.2 shows that the squared Cherenkov angle goes down linearly with the inverse square momentum. The slope of the curve allows a determination of the mass of the particle. Moreover, at saturation where, the momentum is sufficiently larger than the mass of the hypothesis, the square of the saturated angle is simply $\sqrt{2(n-1)}$. This can be simply demonstrate by assuming $\beta = 1$ in the Cherenkov equation.

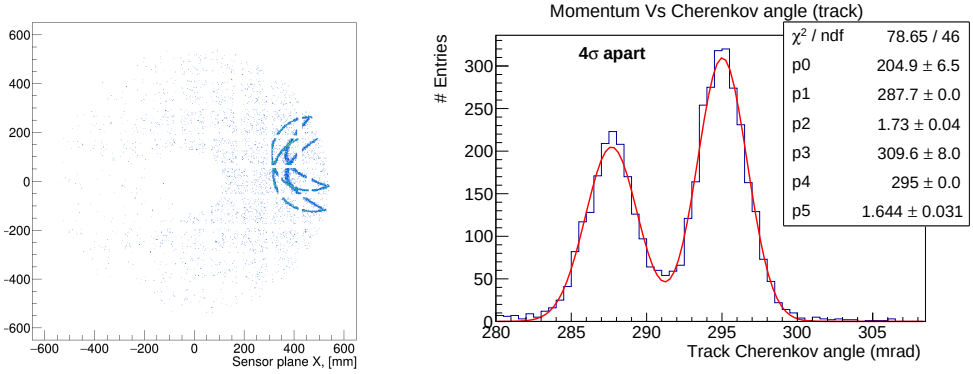

(a) Overlapping rings of pion and kaons (b) Separation of pion and kaons at 7.25 GeV/c

Figure 4.9: Separation of pion and kaon particles with overlapping rings

A number of events with complicated topologies that could be difficult to reconstruct were also studied. For example, Fig. 4.9a presents an event in which a pion and kaon overlap in the critical pseudorapidity region where some fraction of the ring photons stream directly to the photosensors while the rest are reflected back by the mirror. Even for such extreme events, the reconstruction algorithm is capable of at least 4σ separation for pions and kaons with momenta around 7 GeV/c (see Fig. 4.9b).

4.2.5 Kaon detection efficiency and pion rejection

For pions and kaons close to the saturation angle, the pion rejection factor (PRF) as a function of the kaon detection efficiency (KDE) has been estimated by varying the cut applied on the reconstructed track level Cherenkov angle. For 7 GeV/c pions and kaons, generated over a uniform pseudorapidity in the same event, the PRF as a function of KDE is shown in Fig. 4.10. It is seen that one can gain an almost two orders of magnitude increase in PRF (from less than 10 to almost 10^3) by reducing kaon detection efficiency to ~70%. If all particles with a measured track-level Cherenkov angle below 292 mrad (blue line in the left panel of 4.10) are identified as kaons, without any rejection, one can reach a KDE

close to 100%, with a PRF less than 10. However, a cut around 289 mrad would provide 95% KDE with PRF larger than 200. Reducing the cut to even lower values (black line in left panel of 4.10) allows one to reach a PRF close to 10^3, but at a cost of losing 30% of kaons. In physics analyses (discussed in chapter 5), one can therefore improve kaon purity by applying stricter cuts on the reconstructed Cherenkov angle on an event by event basis, as long as the kaon sample is large enough to tolerate a significant fractional loss.

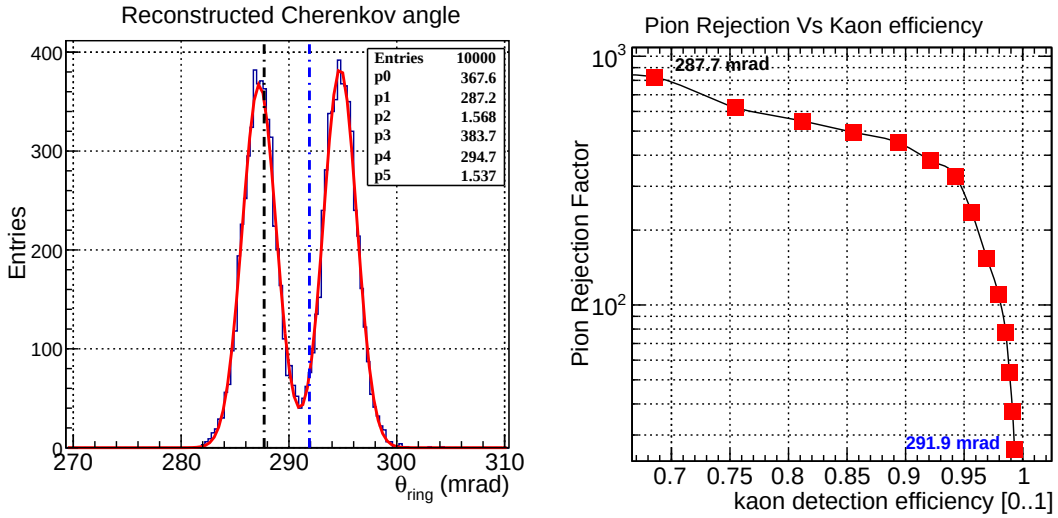

Figure 4.10: Variation of pion rejection factor(PRF) as function of kaon detection efficiency (KDE),is obtained(right panel) varying the Cherenkov theta from 287.7 mrad to 291.9 mrad of the Cherenkov angle distribution (left panel), obtained from 5000 events composed of a pion and a kaon in the same event.

4.2.6 Number of sigma separation

A conventional measure of a RICH detector's performance is the so-called sigma separation count between two mass hypotheses. The process requires precise determination of the track level Cherenkov angular resolution of the particles. Single particle events were generated at different momenta and pseudorapidities for electron, pion, kaon, and proton hypotheses and the resulting Cherenkov angle distributions were fit with a Gaussian from which the mean track level Cherenkov angles and resolutions were extracted. A consitency check has been performed to validate the extracted resolutions (detailed description given in 4.2.3)

The definition of the number of sigma separation between two hypotheses, for example the electron and pion hypotheses, is given by Eq. 4.3. Figure 4.11a presents the electron - pion separation power as a function of particle momentum for three pseudorapidity ranges. It is seen that the separation power is largely independent of pseudorapidity and that a 3σ electron - pion separation is possible up to $\sim$2.5 GeV/c. The statistical uncertainties on the estimations are negligible. The same approach can be performed for pion - kaon separation and the resulting N_σ versus momentum profiles can be seen in Fig. 4.11b. We see that 3σ pion - kaon separation is possible up to $\sim$9 GeV/c.

$$N_\sigma = \frac{\theta_e - \theta\pi}{(\sigma_e + \sigma_\pi)/2} \tag{4.3}$$

Figure 4.11: N_σ separation

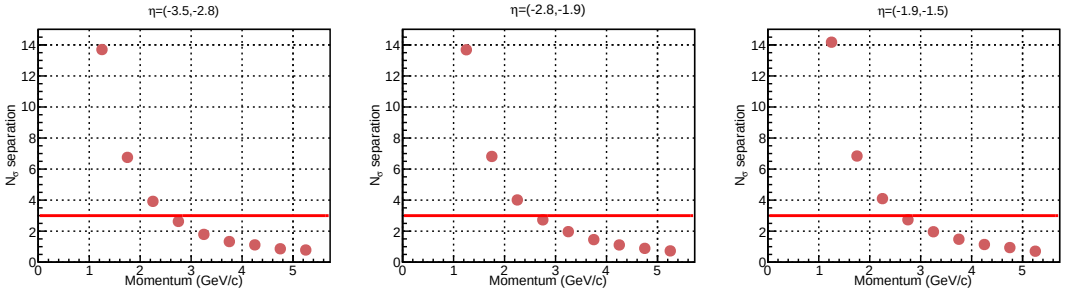

(a) N_σ separation between the electron an pion hypotheses as a function of momentum for different bins of pseudo-rapidity.

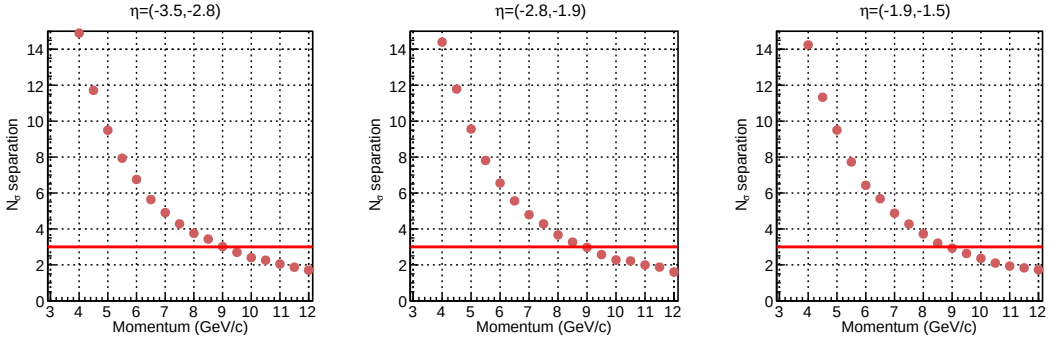

(b) N_σ separation between the pion and kaon hypotheses as a function of momentum for different bins of pseudo-rapidity.

4.3 Timing performance

4.3.1 Collision time from vertex position

Time of flight measurements exploit knowledge of the momentum, path length, and transit time of a particle to determine its mass, and therefore its species. As outlined in Sec. 1.2, the timing capabilities of the pfRICH photosensors could be used to help determine the start time, t_0, for global ToF measurements, especially when the scattered electron falls within the pfRICH acceptance. The properties of the electron and proton bunches as they come into collision allow a complementary method for determining t_0 based on the measurement of the collision vertex position.

The longitudinal size of the electron bunches at the EIC will be much smaller than that of the proton bunches, 0.9 cm versus 6 cm for 18 GeV and 275 GeV electron and proton beams, respectively (values for other energies can be found in Table 3.3 of the EIC Conceptual Design Report [32]). The size discrepancy between the bunches leads to a tight correlation between the collision time and z position of the collision vertex as seen in the left

panel of Fig. 4.12 (the program which simulates the collision reports time and position in millimeters, one can convert to time by dividing by the speed of light, 0.3 mm/ps). Taking a slice of this distribution at a specific z-vertex value and projecting onto the y-axis gives the time resolution achievable by measuring the just the z-vertex. The histogram and red fit in the right panel of Fig. 4.12 shows this resolution is 9 mm or 30 ps. As expected, this is the size of the electron bunch.

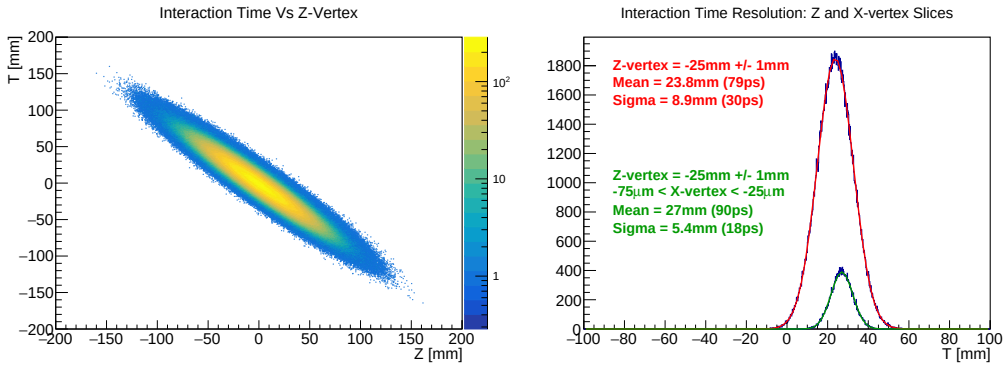

Figure 4.12: (Left) Correlation between t_0 and z-vertex position. (Right) Time distribution for a z-vertex position of $-25 \pm 1\ mm$ (red curve) and the same z-vertex position, but with an additional restriction on the x-vertex position of $-75\ \mu m < \mathrm{x} - \mathrm{vertex} < -25\ \mu m$ (green curve).

An even better t_0 resolution is possible by exploiting the fact that the beams come into collision at an angle while being rotated so that they still pass through each other head-on (see [33] for a more complete description of the beam effects at collision). This implies that the collision point traverses the x-direction (x is in the horizontal plane and perpendicular to the beam) as the bunches pass through one another. Thus, measuring the z-vertex position while simultaneously restricting the position of the x-vertex will act to limit the region of the electron bunch the colliding particle can originate from, improving the achievable t_0 resolution. This can be seen from the green curve in Fig. 4.12, which shows the time projection from the same slice in z as the red curve, but now restricts the x-vertex position to be between $-75\ \mu m$ and $-25\ \mu m$ (a 50 μm x-vertex position resolution should be well within the capabilities of the ePIC vertex detector). It is seen that such a cut improves the t_0 resolution from 30 ps to 18 ps. It should be noted that the model used in this study assumed perfectly gaussian bunch profiles and the presence of non-gaussian tails in the real bunches may degrade this resolution somewhat.

4.3.2 pfRICH Timing Performance

A significant advantage of the pfRICH design is the high fraction of the backward acceptance that is tiled with HRPPDs. HRPPDs, by virtue of the Cherenkov photons produced in the window, can also serve as a precise timing detector. At present, the time resolution of the HRPPDs to incident charged particles is in the process of being understood. In ideal conditions, time resolutions better than 50 ps have been obtained, however, the final performance as implemented in the experiment will depend on a variety of factors such

as clock distribution, electronics implementation, etc. Therefore, the assumption made in the studies presented here is that in the pfRICH the HRPPDs can provide an arrival time measurement for a single photon with a resolution of 50 ps.

Given this time resolution, the acceptance of the pfRICH for performing ToF measurements can be found. Using an assumed time resolution of 50 ps per digitized hit, and assuming that all hits provide an independent measurement of time, to reach the 20 ps level, a detector would need ≥ 6 hits ($\frac{50}{\sqrt{6}} \approx 20$). Requiring 6 hits arriving at a given location also provides a substantial robustness against noise from backgrounds or dark counts.

When a relativistic charged particle traverses the window of the HRPPD, a large number of photons are produced. The Cherenkov threshold in the quartz window is $\beta > \frac{1}{n_{\text{Window}}} \approx 0.6$, which translates into a momentum threshold similar to the traversing particle's mass, i.e $\sim$ 400 keV for electrons, $\sim$ 115 MeV for pions, $\sim$ 800 MeV for protons. Thus, the DIS scattered electron will effectively always produce a signal when it traverses an HRPPD window, and for the purposes of this study it can be assumed to be $\beta \approx 1$. If the electron traverses the center of an HRPPD module, it produces a cone of photons with nominal radius $\sim$ 12 mm. There will also be some photons which totally internally reflect off the photocathode and receive an additional displacement from the nominal impact point. The likelihood of receiving ≥ 6 hits from this case is effectively 100%. The places where this efficiency for receiving hits from window-produced photons drops are at the boundaries between modules, as can be seen from Fig. 4.13. In this simulation, photons which land on the boundary of the HRPPD window are simply absorbed, limiting the number of photons which can be detected for particles incident outside the nominal HRPPD active area to at maximum $\sim$ 50% of the total and the total acceptance for ≥ 6 hits to $\sim$ 90%. However, additional studies were performed in which this surface was metallized to reflect 80% of incident photons, which should be achievable according to the manufacturer (Incom). In this case the acceptance for ≥ 6 hits rose to $\sim$ 95%. This provides a promising option to improve photon detection efficiency, but no studies have yet been performed on the timing performance with this metallization in place. It is worth mentioning that the side facets of the HRPPD quartz window can also be metallized, further increasing the detection efficiency.

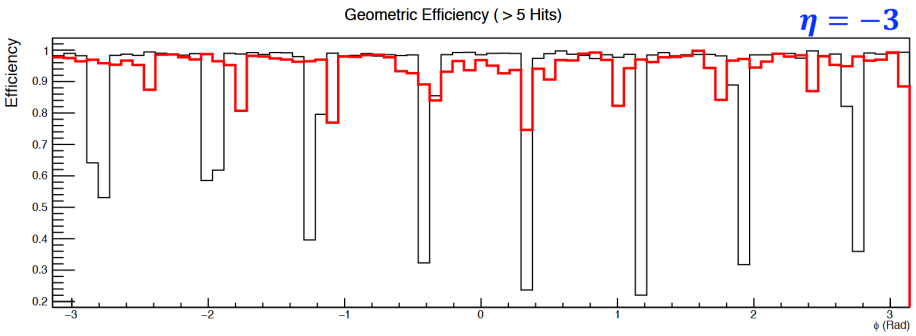

Figure 4.13: Efficiency to receive > 6 hits as a function of primary charged particle azimuthal angle ϕ for only Cherenkov photons originating in the HRPPD window (black) and only photons originating in the aerogel (red).

Photons produced in the window provide the most reliable source of ToF information by virtue of the fact that they are plentiful and traverse only one medium before being detected. However, photons produced in the aerogel, gas, or acrylic filter also carry information about the time that the charged particle arrived at the medium. As shown in Fig. 4.13, the efficiency to detect a significant number of hits from photons produced in the aerogel is even larger than that of the window, by virtue of the fact that the aerogel photons are spread more widely on the sensor plane, and thus are less likely to all fall on inactive regions. The dips in the aerogel efficiency are not due to the HRPPD module boundaries, but instead the ribs of the aerogel support structure. The fact that these two inefficiencies are typically out of phase with one another makes the overall efficiency for the detector to receive greater than 5 hits that can be used for time-of-flight measurements $\sim$ 99%. However, photons originating in the aerogel have a larger degree of ambiguity (refraction at multiple boundaries, material non-uniformity, chromatic effects, etc.) and will therefore on average have a worse time resolution. An ideal timing reconstruction algorithm therefore would likely give these photons a lower weight compared to the window photons, if they are available.

4.4 Tracking Parameterization

The performance of the RICH detector will depend on how well the ePIC tracking system can measure the momenta and angular positions of the reconstructed tracks. The momentum and angular resolutions were evaluated in the ePIC tracking system and then parameterized as a function of momentum for several pseudorapidity values spanning a range from -1.80 to -3.41. The simulation was done within the official ePIC software stack using the Bryce Canyon geometry configuration. A particle gun was used to simulate π^- particles at fixed values of momentum, polar angle (θ) and azimuthal angle (ϕ). The tracks were then reconstructed using a truth seeded version of ACTS and then propagated to a pseudo detector plane located at $z = -1200\ mm$, where the spread in the momentum and angular distributions were taken as the resolutions at the location of the pfRICH detector. For each pseudorapidity setting the respective resolutions were plotted versus momentum and the momentum and angular resolutions were parameterized with a function of the form $f(p) = \sqrt{(Ap)^2 + B^2}$ and $fp = \sqrt{(A/p)^2 + B^2}$, respectively. These results were cross-checked with ePIC performance studies and found to be consistent. Figure 4.14 shows the momentum and angular resolutions projected to $z = -1200mm$ and the fit used for the parameterization at $\eta = -2.0$

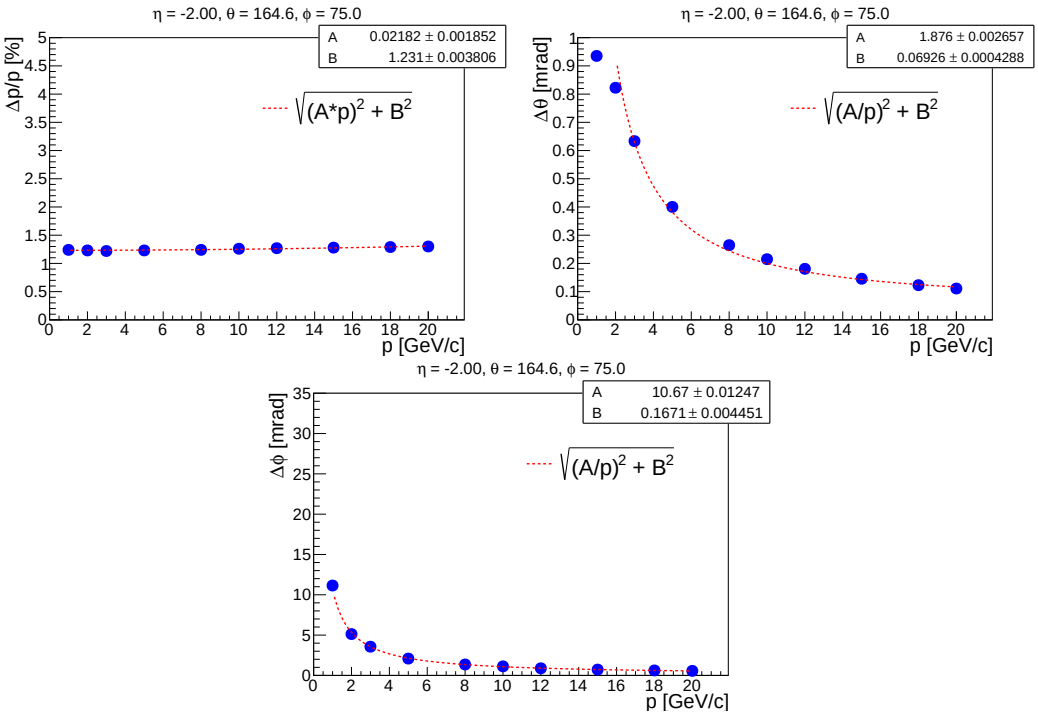

Figure 4.14: Representative example of momentum (top-left), polar angle (top-right), and azimuthal angle (bottom) resolutions projected to a surface at $z = -1200mm$ vs. momentum and the fit used for parameterization (red dashed line) of the performance. These results are for π^- particles at $\eta = -2.0$, $\theta = 164.4^o$, and $\phi = 75.0^o$.

Chapter 5

Physics Performance

5.1 Electron/pion separation

One of the key functions of the pfRICH will be to assist with the identification of scattered electrons in the momentum region where the electromagnetic calorimeter can no longer be used efficiently ($p < 5\,\mathrm{GeV}/c$). The dominant background to the scattered electrons in this region are π^- mesons, so this study focuses on electron/pion separation power of the pfRICH using PYTHIA-6 ep collisions at 18×275 GeV. The use of simulated events from a Monte Carlo event generator ensures realistic electron and pion yields.

The importance of good PID in this kinematic region is demonstrated in Fig. 5.1, which shows that the expected π^- multiplicities (open black squares) are much larger than those of the scattered electrons (full red circles). In order to evaluate the electron-pion separation power of the pfRICH, a table with PID probabilities of electrons and pions was used. These probabilites, listed for several momentum and pseudorapidity values, were calculated using the reconstruction software described in Sec. 4.1. The table assumes 100% PID efficiency for both particle species. The green squares then represent pions suppressed by a factor calculated from the PID table, taking into account both probabilities of correctly identifying e and π, as well as their mis-identification.

Under these assumptions, the pfRICH can provide good pion suppression at momenta $p < 2\,\mathrm{GeV}/c$, as can be seen in Fig. 5.2. At higher momenta, the suppression power is not sufficient to distinguish between electrons and pions. This range can be extended by introducing a momentum-dependent cut on the Cherenkov angle measured by pfRICH. As a result, the reconstruction efficiency of given particle species will decrease, but the sample purity will be improved. The ability to perform such a selection is currently being implemented in the pfRICH simulation framework.

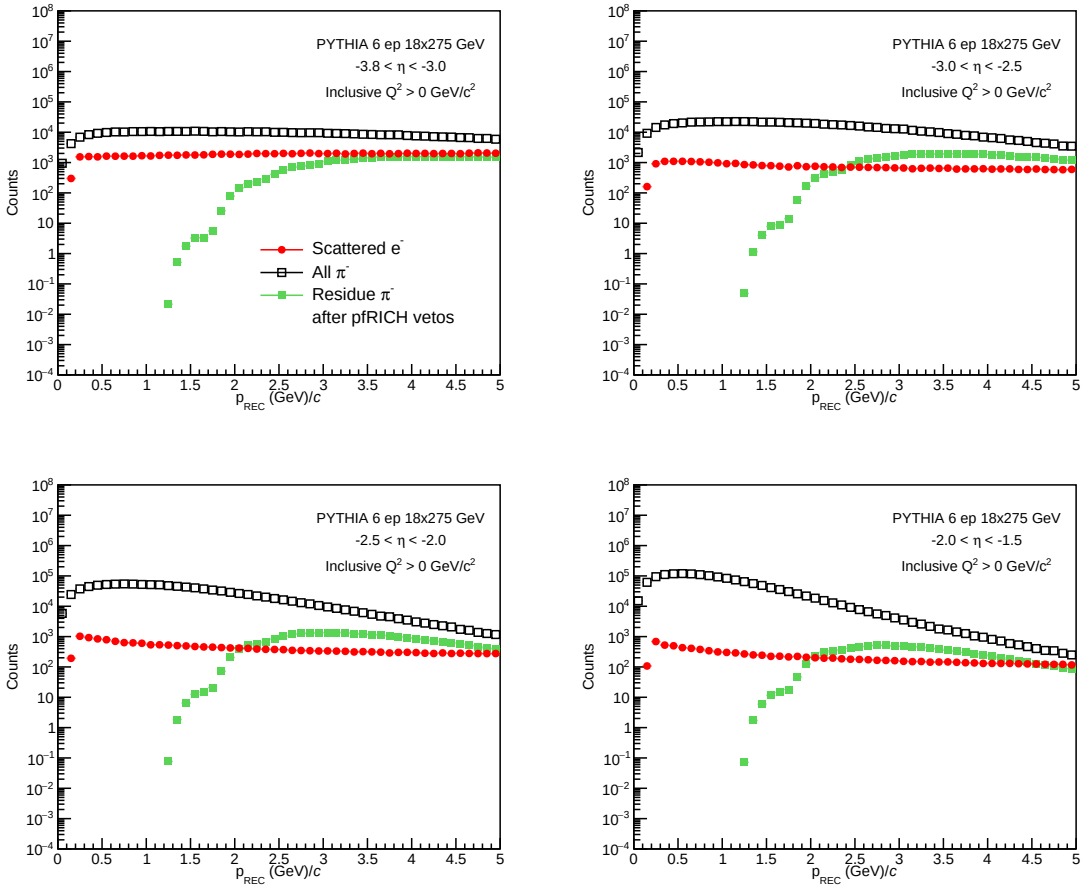

Figure 5.1: Scattered electron momentum distributions in PYTHIA 6 ep collisions at 18 × 275 GeV compared to π^- before (open black squares) and after (green full squares) pfRICH veto in four η bins, covering full pfRICH η acceptance.

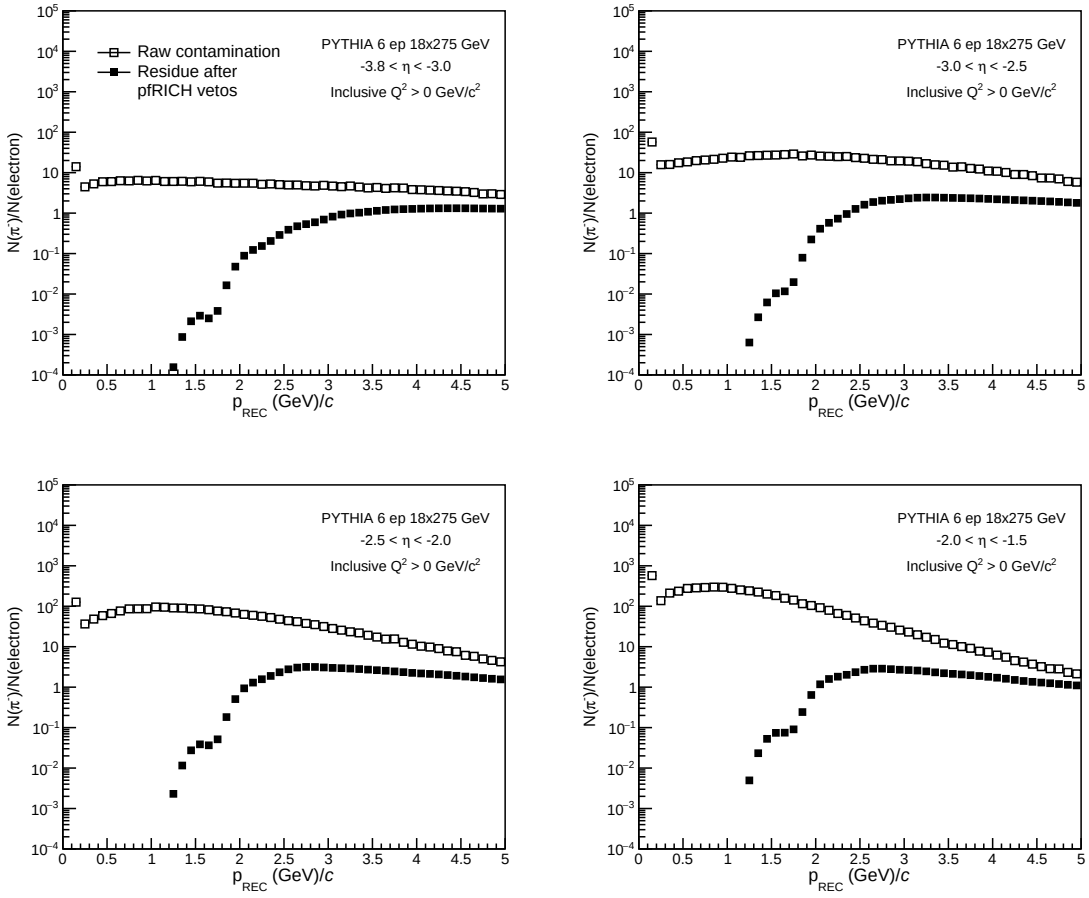

Figure 5.2: Yield ratios of $\pi^-/e_{\rm scat}$ before (open black squares) and after (black full squares) pfRICH veto on π^- in PYTHIA 6 ep collisions at 18×275 GeV for four η bins, covering full pfRICH η acceptance.

5.2 SIDIS Impact Study

The ability to separate and identify different hadron species is a key requirement for many SIDIS analyses. The hadron PID capabilities of the pfRICH are evaluated here via reconstruction of leading K^- particles. This study is divided into two parts: (1) the multiplicities of leading momentum K^-s are evaluated in various (Q^2, y) bins in order to determine regions of phase space where the pfRICH can be used to identify K^- mesons and (2) the K^- selection purity is evaluated within these regions. The study is performed using ePIC full simulation of DIS ep collisions at 18×275 GeV, combined with the $\pi/K/p$ pfRICH PID probability table.

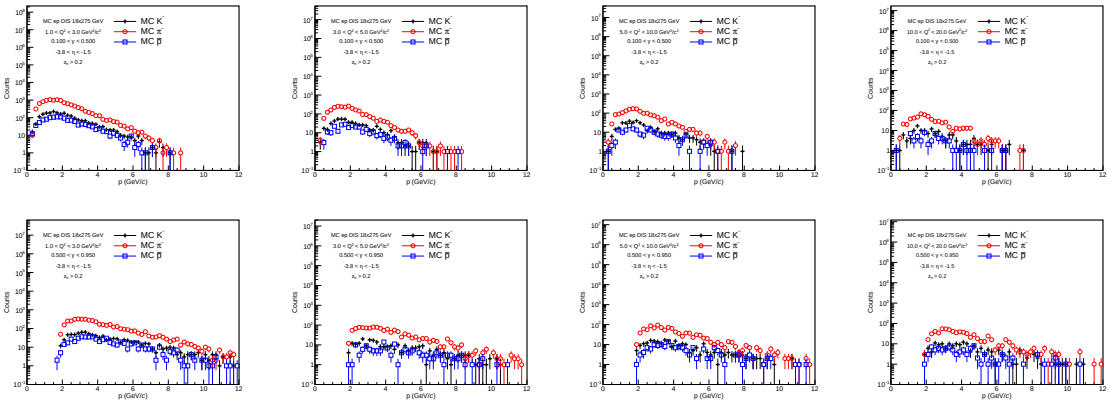

Figure 5.3: Yields of true MC negative pions (red empty circles), kaons (black full crosses), and anti-protons (blue empty squares) with $z_\mathrm{h} > 0.2$ as a function of momentum from ePIC full simulation of DIS ep collisions at 18×275 GeV in multiple (Q^2, y) bins. The top row shows the spectra for $0.1 < y < 0.5$, while the bottom row for $0.5 < y < 0.9$. The columns show bins in Q^2, from left to right: $1 < Q^2 < 3\,\mathrm{GeV}^2/c^2$, $3 < Q^2 < 5\,\mathrm{GeV}^2/c^2$, $5 < Q^2 < 10\,\mathrm{GeV}^2/c^2$, and $10 < Q^2 < 20\,\mathrm{GeV}^2/c^2$.

First, the leading hadrons are selected using Lorentz-invariant variable z_h defined as

$$z_\mathrm{h} = \frac{P \cdot p_\mathrm{h}}{P \cdot q}, \tag{5.1}$$

where P is the momentum of the beam proton, q is the momentum of the photon, and p_h is the momentum of the final state hadron. The yields of true MC π^-, K^-, and $\bar{p}$ particles with $z_\mathrm{h} > 0.2$ as a function of momentum for different kinematic bins are shown in Fig. 5.3. Both π^- and $\bar{p}$ are significant backgrounds to K^-, meaning good hadron PID capabilities will be necessary for analyses requiring a pure kaon sample.

Identification of K^-s using the pfRICH is done in the reconstructed charged tracks from ePIC full simulation utilizing the $\pi/K/p$ PID probability table containing both the probabilities of correctly identifying K^-s as K^-s and misidentifying π^-s or $\bar{p}$s as K^-s. The K^- candidates (all particles identified as Kaons by the pfRICH) selected using this method are shown in Fig. 5.4 as green full squares. The selected candidates are dominated by correctly identified K^-s (pink open squares) for $2 < p < 6\,\mathrm{GeV}/c$. At larger momentum, there is a

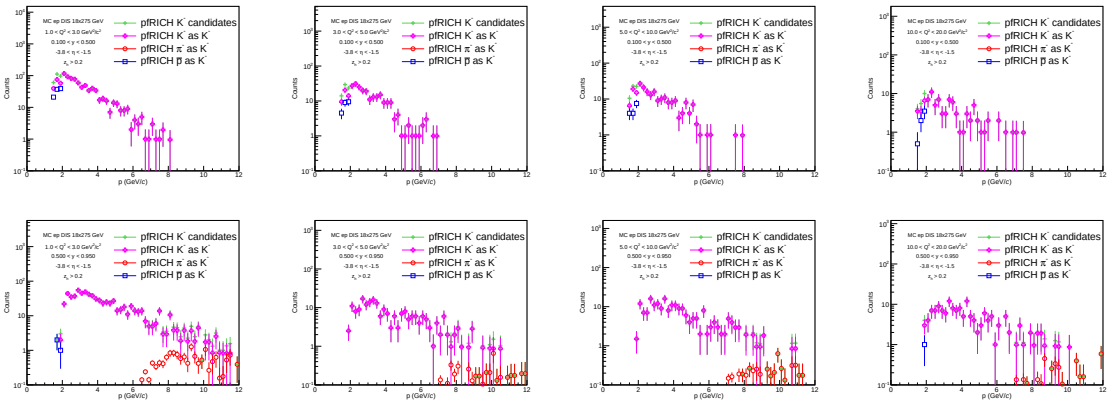

Figure 5.4: Leading K^- candidates as a function of momentum selected from the reconstructed charged tracks in ePIC full simulation of DIS ep collisions at 18×275 GeV in multiple (Q^2, y) bins. Only K^-s inside the pfRCIH η acceptance ($-3.8 < \eta < -1.5$) are shown. All K^- candidates (full green crosses) are compared to correctly identified K^- (pink open crosses), as well as to π^-s (red open circles) and $\bar{p}$s (blue open squares) misidentified as K^-s. The top row shows the spectra for $0.1 < y < 0.5$, while the bottom row for $0.5 < y < 0.9$. The columns show bins in Q^2, from left to right: $1 < Q^2 < 3\,\mathrm{GeV}^2/c^2$, $3 < Q^2 < 5\,\mathrm{GeV}^2/c^2$, $5 < Q^2 < 10\,\mathrm{GeV}^2/c^2$, and $10 < Q^2 < 20\,\mathrm{GeV}^2/c^2$.

rising contribution from π^-s misidentified as K^-s (red open circles). The background from incorrectly identified $\bar{p}$s (blue open squares) is small over the whole momentum range.

The purity of the selected K^- candidates a function of momentum is shown in Fig. 5.5. Here, purity is defined as

$$\text{Purity} = \frac{N_{K^-}}{N_{K^-} + N_{\pi^-} + N_{\bar{p}}}, \tag{5.2}$$

where N_{K^-} is the multiplicity of correctly identified kaons and N_{π^-} and $N_{\bar{p}}$ are the numbers of pions and anti-protons misidentified as kaons, respectively. The pfRICH performance is best in the region $2 < p < 6\,\mathrm{GeV}/c$, where the sample purity is reaching nearly 100%. Despite the rising contribution of misidentified π^-s for $p > 6\,\mathrm{GeV}/c$, the purity stays above 80% up to $p < 10\,\mathrm{GeV}/c$. Only for higher momentum does the K^- purity drop significantly, which is primarily driven by very low statistics of K^- and rising misidentification probability of other hadrons.

Overall, the pfRICH is able to provide excellent K^- identification performance in the negative η region for momenta within $2 < p < 6\,\mathrm{GeV}/c$, where the selected sample purity is close to 100%. As a result, the pfRICH detector can significantly contribute to SIDIS analyses requiring identification of leading K^-s.

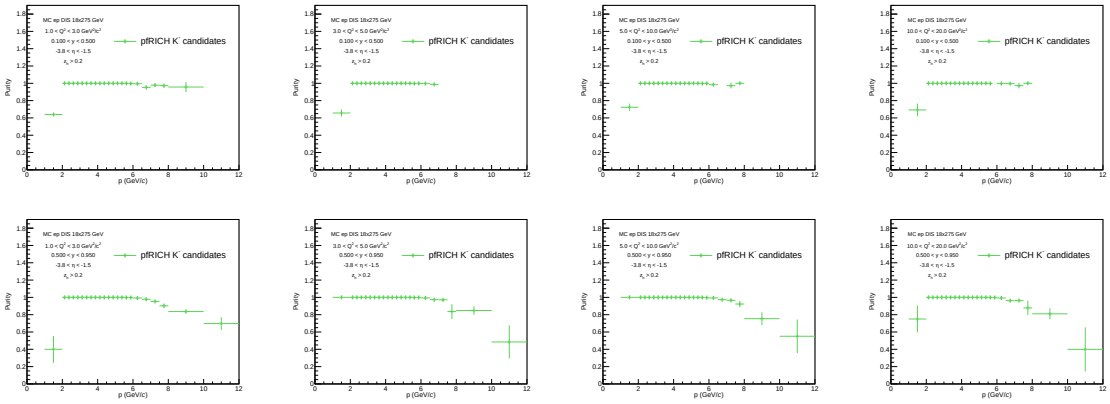

Figure 5.5: Purity of selected K^- candidates a function of momentum in in ePIC full simulation of DIS ep collisions at 18×275 GeV in multiple (Q^2, y) bins. The top row shows the purity for $0.1 < y < 0.5$, while the bottom row for $0.5 < y < 0.9$. The columns show bins in Q^2, from left to right: $1 < Q^2 < 3\,\mathrm{GeV}^2/c^2$, $3 < Q^2 < 5\,\mathrm{GeV}^2/c^2$, $5 < Q^2 < 10\,\mathrm{GeV}^2/c^2$, and $10 < Q^2 < 20\,\mathrm{GeV}^2/c^2$.

Chapter 6

Cost, Schedule and Workforce

6.1 Cost

Material costs were estimated precisely, based on the composition of the pfRICH detector, as presented in this document:

- Vessel cost (honeycomb carbon fiber sandwich walls and aluminum mounting plate) estimates were derived from the recent orders placed during construction of the sPHENIX TPC
- Aerogel and mirror cost estimates were provided by the manufacturers (Chiba aerogel Factory and CMA, respectively)
- HRPPD costs were derived from a public presentation by the manufacturer (Incom) and confirmed during a recent meeting between the EIC leadership teaam and Incom in Charlton, MA in January 2023
- High Voltage and Low Voltage system costs are based on the manufacturer quotes (CAEN and Wiener, respectively)
- Cooling system costing is mostly based on the catalogue items and off the shelf parts
- Gas system evaluation is based on experts' prior experience building a similar setup
- ASIC and FEB cost estimates are merely projections at this point, however scaling with channel count is incorporated in all estimates
- HRPPD QA station equipment is a replica of a similar test stand at Incom, where a detailed cost breakdown was provided to us
- The aerogel QA station equipment list was composed based on our present understanding of what this system should consist of, and a subsequent market search

Labor costs are merely rough estimates at this point, based on the input provided by various experts reflecting their experience of building similar detectors in the past. The pfRICH detector cost breakdowns into various categories are given in Fig. 6.1.

Sub-system	In-Kind Material	Project Material	Total Material	In-Kind Labor	Project Labor	Total Labor	Total
pfRICH protyping and beam tests	$10,020	$44,980	$55,000	$0	$50,788	$50,788	$105,788
pfRICH Final Design	$0	$0	$0	$0	$1,515,192	$1,515,192	$1,515,192
pfRICH production - HV system	$0	$281,495	$281,495	$0	$0	$0	$281,495
pfRICH production - LV system	$0	$29,600	$29,600	$0	$0	$0	$29,600
pfRICH production - Gas system	$0	$13,400	$13,400	$0	$0	$0	$13,400
pfRICH production - Cooling system	$0	$42,650	$42,650	$0	$0	$0	$42,650
pfRICH production - Photosensors	$0	$1,360,000	$1,360,000	$0	$0	$0	$1,360,000
pfRICH production - ASIC FE cards and RDOs	$0	$44,775	$44,775	$0	$0	$0	$44,775
pfRICH production - Vessel	$80,000	$57,000	$137,000	$0	$0	$0	$137,000
pfRICH production - Mirrors	$0	$351,000	$351,000	$0	$0	$0	$351,000
pfRICH production - Aerogel	$0	$180,600	$180,600	$0	$0	$0	$180,600
pfRICH Aerogel QA test station	$0	$32,500	$32,500	$6,400	$22,717	$29,117	$61,617
pfRICH HRPPD QA test station	$0	$160,500	$160,500	$0	$314,100	$314,100	$474,600
pfRICH assembly and installation	$0	$60,000	$60,000	$0	$612,718	$612,718	$672,718
Total	$90,020	$2,658,500	$2,748,520	$6,400	$2,515,514	$2,521,914	$5,270,434

Figure 6.1: pfRICH cost breakdown.

The overall budget is shown in Fig. 6.2. Total detector cost in 2023 US dollars amounts to ∼5.3M, almost equally shared between material and labor costs. The "Expert opinion" category in Fig. 6.2 is only related to labor estimates. Detailed costing information exists as an Excel file with a format closely resembling the project WBS costing sheets layout.

Sub-system: PID pfRICH	In-Kind	Project	Total	
Material ($)	$90,020	$2,658,500	$2,748,520	52%
Labor ($)	$6,400	$2,515,514	$2,521,914	48%
Total ($)	$96,420	$5,174,014	$5,270,434	
	93%	51%		
	7%	49%		

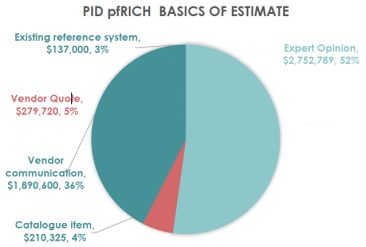

Figure 6.2: pfRICH costs broken down into material and labor, with project and in-kind contributions listed separately (left) and the basis of estimate (right).

6.2 Schedule

The pfRICH design and construction schedule is shown in Fig. 6.3. It is based on the assumption that material purchases can start right after the anticipated CD-3 stage of the EIC project is reached, namely in early summer 2025. The end date is based on the requirement to have the detector installed well ahead of the CD-4a early finish date of April 3031 and will need further tuning depending on other ePIC subsystem installation schedules. It should be noted that according to manufacturer feedback, none of the expected procurement will take more than two years of time.

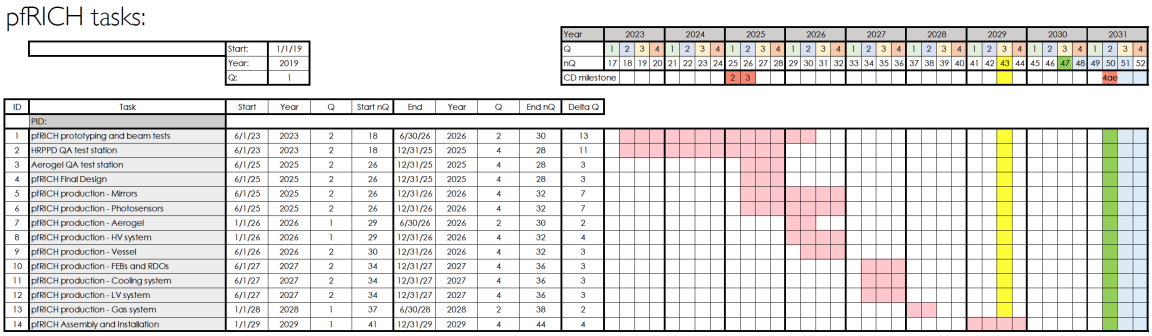

Figure 6.3: pfRICH design and construction schedule, synchronized with the EIC project timelines.

6.3 Institutions and Workforce

Several institutions and individuals contributed to this CDR to date. Figure. 6.4 summarizes their present and expected future activities, as well as the level of commitment to the pfRICH Detector SubSystem Collaboration (DSSC).

	Current and expected participation in pfRICH	Comment
Brookhaven National Lab	Default site for HRPPD QA station Gas, cooling, HV & LV systems, DAQ Detector and physics modeling Beam tests	
Chiba University	Connection to Chiba Aerogel Factory	No institutional commitment
Duke University	Software support Physics modeling	
INFN Genova	Detector modeling, beam tests, LV & HV system design	Until CD-3
INFN Trieste	Detector modeling, beam tests	Until CD-3
Jefferson Lab	Mechanical design	Project engineering support
Ljubljana University and JSI	Expert input on detector design	No institutional commitment
Mississippi State University	Beam test participation and data analysis	Until June 2023
Stony Brook University	Vessel design and production Potential pfRICH construction site Beam tests	
Temple University	Aerogel QA station	
Yale University	Potential site for HRPPD QA station	

Figure 6.4: pfRICH DSSC institutions as of March 2023.

Chapter 7

Research and Development Plans

7.1 Proximity focusing RICH technology

The technology of proximity focusing RICH detectors using non-gaseous radiators is well established in the fields of high-energy particle and nuclear physics. They were successfully operated either alone, e.g, Belle II and ALICE, or in combination with a gaseous RICH (dual RICH) in many experiment, e.g. HERMES and LHCb (the latter two in a combination with focusing mirrors). Consequently, no R&D is necessary for the concept of the pfRICH itself.

7.2 Dual aerogel configuration

The ePIC pfRICH baseline configuration meets the Yellow Report requirements and has only one 2.5 cm thick aerogel layer with a refractive index of ~ 1.045. Should a further boost in performance become necessary, the preliminary Monte-Carlo simulations showed that one can successfully make use of a dual-aerogel configuration, in particular in a so-called defocusing configuration. The concept of using multi-layer aerogel radiators was brought up in the early 2000s by Samo Korpar and Toru Iijima. In collaboration with the Ljubljana group lead by Peter Krizan, the first successful beam tests were carried out in 2004 [34]. A follow-up study on the robustness of the method, sensitivity to momentum, and difference of the two refractive indices further established the feasibility of this approach [35]. In parallel to this effort, the group in Novosibirsk also had a similar idea, and a 2006 joint paper [36] summarized the combined effort. The focus then shifted to dedicated R&D for the Belle II RICH in the forward region. These efforts concluded with the construction of the detector in 2017 [37]. The dual-radiator RICH counter in Belle II (known as ARICH) covers the range of impact angles between 17 and 35 degrees. It works to specifications and is operated successfully. Studies of multi-layer aerogel radiators, especially by the Ljubljana group, continue to-date. Given the expertise of this group we conclude that no project specific R&D is necessary, with the obvious exception of one or a few prototype test beams.

7.3 HRPPDs

While the general pfRICH concept itself will not need further R&D, the HRPPD photosensors themselves and their corresponding ASIC readout electronics will require focused R&D effort. R&D for HRPPD is the subject of the eRD110 consortium that is funded through the EIC Project.

7.3.1 Institutional responsibilities

The HRPPD evaluation process for ePIC is seen as a coordinated effort between Argonne National Laboratory (ANL), Brookhaven National Laboratory (BNL), Istituto Nazionale di Fisica Nucleare (INFN) Trieste and Genova, and Mississippi State University (MSU) in close contact with Incom. Magnetic field tolerance studies are performed by the ANL group using g-2 calibration magnet equipment. Pixellation and position-resolution studies are primarily performed by BNL, adapting the existing equipment and the readout board designs to the state-of-the-art HRPPD tiles of different types (10 cm and 20 cm size, capacitively and directly coupled readout). The single- and multi-photon timing resolution measurements (essential for the imaging Cherenkov detectors and Time-of-Flight application, respectively) are the primary focus of INFN Trieste and Genova. This effort requires tedious calibration of the existing DRS4 electronics, and will be performed in collaboration with INFN Bologna, using substantial base funding from the EIC NET Collaboration in Italy. INFN and MSU will provide the majority of the manpower for the bench and beam test data analysis. All groups are expected to join the beam tests at FNAL and / or CERN to evaluate the sensor behaviour under beam conditions.

7.3.2 R&D plan for FY23

The current work plan foresees activity in the following areas:

- Development of the mechanical and electrical interface to the HRPPDs with direct pixel readout.
- Tests of HRPPDs in a high magnetic field oriented at non-zero angles to the detector plane, specific to the particular anticipated locations of these sensors in the ePIC detector PID subsystems.
- Further HRPPD spatial and timing resolution optimization for different pad sizes, also using moderate low-noise signal preamplification.

In addition to efforts within eRD110, the pfRICH team will support Incom in its effort to improve the mechanical and electronic engineering aspects of the HRPPDs to better fit ePIC's needs.

7.3.3 Preview of remaining R&D in FY24

The mechanical and electrical interface to the HRPPD with a direct readout may require further iterations using custom low force spring loaded LGA sockets. Beam tests with a pfRICH prototype equipped with a selected HRPPD photosensor are foreseen. In addition,

the newest Incom state-of-the-art HRPPD models at that time may require separate evaluation and a joint effort with eRD109 in building an integrated sensor+ASIC board assembly is needed in FY24.

7.4 ASICs and Front End Electronics

The development of ASICs and FEEs are coordinated by eRD109. At the time of the writing of this proposal, efforts towards the development of ASICs and FEEs have only just started. The FY23 R&D proposal of eRD109 did not include HRPPD specific resources because the decision to make HRPPDs the baseline for the backward RICH detector came after the proposal deadline. Discussions with eRD109 and the Project are underway.

Just recently [38], an ad hoc meeting initiated by pfRICH members and management of the eRD109 consortium, and attended by detector experts and ASIC developers, came to a conclusion that the EICROC ASIC, which is under active development for ePIC AC-LGAD ToF detectors, should meet the HRPPD photosensor requirements in terms of collected charge, detector capacitance and anticipated timing resolution. Therefore, the pfRICH design presented in this proposal assumes EICROC ASIC usage. As a consequence, the Low Voltage setup, Cooling System, and Front End Board (FEB) configuration were designed and evaluated using the EICROC target specifications in a 256-channel configuration.

Acknowledgments

References

[1] R. Abdul Khalek, et al., Science Requirements and Detector Concepts for the Electron-Ion Collider: EIC Yellow Report, Nucl. Phys. A 1026 (2022) 122447. arXiv:2103.05419, doi:10.1016/j.nuclphysa.2022.122447.

[2] EIC Geometry Database, https://eic.jlab.org/Geometry/Detector/.

[3] H. Klest, et al., Overview and design of sPHENIX TPC, J.Phys.Conf.Ser. 1498 (2020) 012025. doi:10.1088/1742-6596/1498/1/012025.

[4] Chiba Aerogel Factory Co., Ltd., https://www.aerogel-factory.jp/.

[5] M. Yonenaga, et al., Performance evaluation of the aerogel RICH counter for the Belle II spectrometer using early beam collision data, Prog. Theor. Exp. Phys. (093H01) (2020). doi:10.1093/ptep/ptaa090.

[6] M. Tabata, H. Kawai, Progress in Development of Silica Aerogel for Particle- and Nuclear-Physics Experiments at J-PARC, JPS Conference Proceedings (8) (2015) 022004. doi:https://doi.org/10.7566/JPSCP.8.022004.

[7] O. H. W. Siegmund, et al., Advances in microchannel plates and photocathodes for ultraviolet photon counting detectors, Society of Photo-Optical Instrumentation Engineers Proceedings 81450J. doi:https://doi.org/10.1117/12.894374.
URL https://incomusa.com/wp-content/uploads/Advances-in-Microchannel-Plates-and-Photoca
pdf

[8] C. J. Hamel, et al., LAPPD and HRPPD: Upcoming Upgrades to Incom's Fast Photosensors.
URL https://indico.bnl.gov/event/17475/contributions/69807/attachments/44033/74296/EIC%20SBIR%20for%20LAPPD%20Community%20Workshop.pdf

[9] Development of Advanced Photocathode Materials for LAPPD, https://www.sbir.gov/sbirsearch/detail/1863407.

[10] Techtra, http://www.techtra.pl.

[11] Samter high density compression interposers, http://suddendocs.samtec.com/catalog_english/za1.pdf.

[12] EICROC ASIC, https://indico.bnl.gov/event/18539/contributions/73731/attachments/46348/78403/CdLT_EICROC_6mar23.pdf.

[13] Organization for Micro-Electronics desiGn and Applications, https://portail.polytechnique.edu/omega/.

[14] J. Anderson, et al., FELIX: a PCIe based high-throughput approach for interfacing front-end and trigger electronics in the ATLAS Upgrade framework, JINST 11 (12) (2016) C12023. doi:10.1088/1748-0221/11/12/C12023.

[15] ATHENA Beam Background Estimations, https://wiki.bnl.gov/athena/index.php?title=Beam_backgrounds.

[16] CAEN A1515BV 16-channel floating ground High Voltage module, https://www.caen.it/products/a1515b/.

[17] CAEN SY4527 High Voltage mainframe, https://www.caen.it/products/SY4527/.

[18] Wiener Mpod Low Voltage system, https://www.wiener-d.com/power-supplies/mpod-lv-hv/.

[19] Custom pfRICH Software Suite, https://github.com/alexander-kiselev/pfRICH.

[20] S. Agostinelli, et al., GEANT4—a simulation toolkit, Nucl. Instrum. Meth. A 506 (2003) 250. doi:10.1016/S0168-9002(03)01368-8.

[21] R. Brun, F. Rademakers, ROOT - An Object Oriented Data Analysis Framework, Proceedings AIHENP'96 Workshop, Lausanne, Nucl. Inst. & Meth. in Phys. Res. A (389) (1997) 81–86. doi:10.5281/zenodo.3895855.

[22] ePIC IRT Package, https://github.com/eic/irt/tree/pfrich.

[23] Composite Mirror Applications, https://www.compositemirrors.com/.

[24] ePIC Solenoid Field Map at 2T, https://wiki.bnl.gov/EPIC/images/f/f5/MARCO_v.6.4.1.1.3_2T_Magnetic_Field_Map_2022_11_14_rad_coords_cm_T.txt.

[25] Aerogel optical parameters used in GEANT simulation, https://github.com/alexander-kiselev/pfRICH/blob/main/database/BelleII.xml.

[26] Acrylic filter optical parameters used in GEANT simulation, https://github.com/alexander-kiselev/pfRICH/blob/main/g4irt/include/g4dRIChOptics.hh#L387.

[27] Nitrogen optical parameters used in GEANT simulation, https://github.com/alexander-kiselev/pfRICH/blob/main/source/Materials.cc#L84.

[28] HRPPD quartz window optical parameters used in GEANT simulation, https://github.com/alexander-kiselev/pfRICH/blob/main/database/RefractiveIndex.txt.

[29] FairRoot: A simulation, reconstruction and analysis framework that is based on the ROOT system., https://github.com/FairRootGroup/FairRoot.

[30] C. Pinkenburg, Fun4All Simulation Framework.
URL https://github.com/eic/fun4all_coresoftware

[31] S. Baker, R. Cousins, Clarification of the Use of Chi Square and Likelihood Functions in Fits to Histograms, Nucl.Instrum.Meth. (221) (1984) 437. doi:10.1016/0167-5087(84)90016-4.

[32] F. Willeke, J. Beebe-Wang, Electron ion collider conceptual design report 2021 (2 2021). doi:10.2172/1765663.
URL https://www.osti.gov/biblio/1765663

[33] Accelerator and beam conditions critical for physics and detector simulations for the Electron-Ion Collider, https://doi.org/10.5281/zenodo.6514605.

[34] T. Iijima, et al., A Novel type of proximity focusing RICH counter with multiple refractive index aerogel radiator, Nucl. Instrum. Meth. A 548 (2005) 383–390. arXiv:physics/0504220, doi:10.1016/j.nima.2005.05.030.

[35] P. Krizan, S. Korpar, T. Iijima, Study of a nonhomogeneous aerogel radiator in a proximity focusing RICH detector, Nucl. Instrum. Meth. A 565 (2006) 457–462. arXiv:physics/0603022, doi:10.1016/j.nima.2006.05.233.

[36] A. Y. Barnyakov, et al., Cherenkov Detector with a Focusing Aerogel Radiator, eConf C0604032 (2006) 0045.

[37] R. Pestotnik, et al., The aerogel Ring Imaging Cherenkov system at the Belle II spectrometer, Nucl. Instrum. Meth. A 876 (2017) 265–268. doi:10.1016/j.nima.2017.04.043.

[38] Meeting between ePIC Cherenkov PID detector representatives, MCP-PMT experts and EICROC ASIC designers, https://indico.bnl.gov/event/18539/.

Appendix

e/π Separation Using threshold Cherenkov radiation in Gas

The expansion volume of pfRICH is filled with gas that can produce Cherenkov radiation for certain particle velocities. This emission can be used as a threshold Cherenkov detector to identify low momentum electrons.

The default option for the expansion volume gas is nitrogen, which is UV-transparent and easy to handle. It has a pion Cherenkov threshold of about 4.9 GeV/c, however the small refractive index has significant drawbacks: it generates a small number of Cherenkov photons and the Cherenkov angle in nitrogen is very small (about 1.4 degrees). In fact, GEANT4 simulations (see Figs. 7.1 and 7.2) show that the average number of photo-electrons produced by nitrogen Cherenkov photons is about 7 and they overlap completely with the Cherenkov photons generated in the HRPPD quartz window (about 85 p.e. on average).

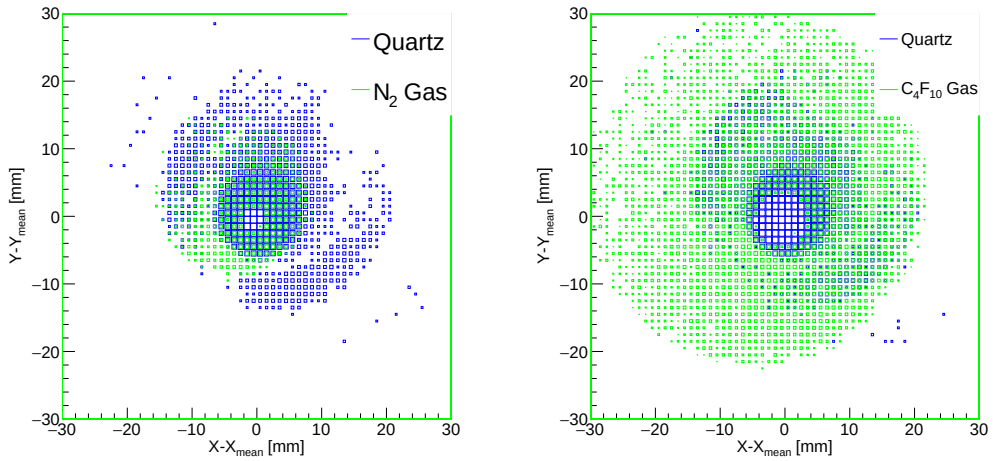

Figure 7.1: Relative impact point of detected photons on the sensor plane for N_2 (left) and C_4F_{10} (right) gases in the expansion volume. Blue and green boxes show the contribution of Cherenkov photons produced in the HRPPD window and gas, respectively.

Furthermore, gas photons give the same timing as window photons within 1 ps (see Fig. 7.3). Therefore, nitrogen Cherenkov photon are completely indistinguishable from the far more abundant HRPPD window Cherenkov photons, even though the charged particle trajectory bending helps to somewhat separate these two groups of photons.

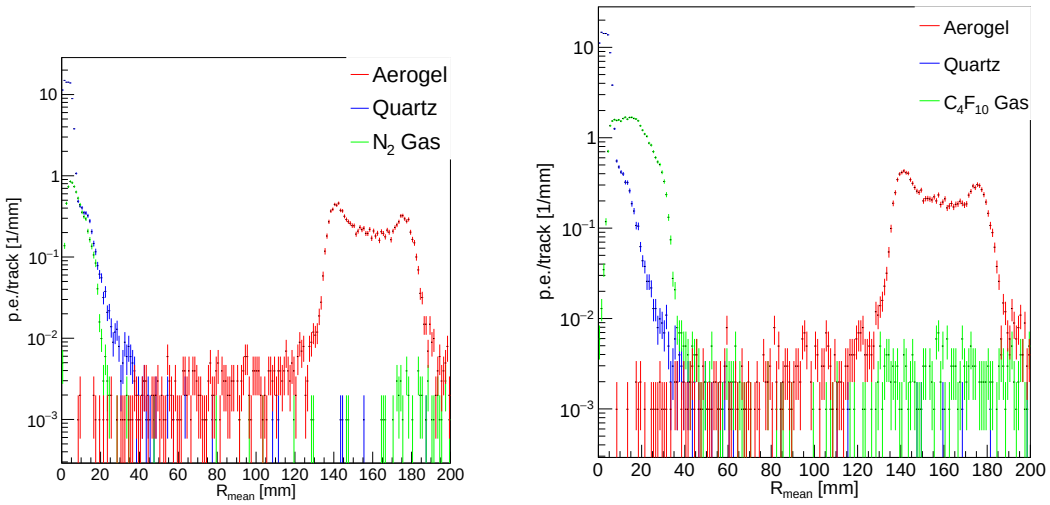

Figure 7.2: 1D-projection of the radius of the Fig.7.1, but extended to include the aerogel photon region.

Larger Cherenkov angles and higher photon yields can be obtained using n perflourcarbons. We have simulated C_2F_6 and C_4F_{10} gases in the pfRICH expansion volume. The C_2F_6 radiator gives ∼17 p.e., but a Cherenkov angle that is still too small, such that the electron-pion separation can be performed only at the level of about 2σ up to momenta of 3.5 GeV/c. In the case of C_4F_{10} gas, which has a typical refractive index of $n = 1.0014$ and a pion threshold of 2.8 GeV/c, we obtained ∼33 p.e. and $> 4\sigma$ electron-pion separation up to 3 GeV/c.

However, C_4F_{10} is fairly expensive, requires a sophisticated purification system and special type of mirrors, while electron-pion separation using aerogel is readily available up to ∼2.5 GeV/c at a 3σ level. Heavier gases, such as the C_5F_{12}, used in DELPHI and SLD require heating, which is challenging from an integration standpoint and introduces further complications. We therefore decided to use nitrogen as the expansion volume gas for the purposes of this CDR.

The contamination of Cherenkov photons produced in N_2 gas into the spacial region of aerogel photons was estimated to be $< 0.4\%$ (see Fig. 7.3), this number increases up to about 2% for C_4F_{10}. However, in both cases the contamination is much smaller than statistical fluctuations of the number of detected Cherenkov photons produced in aerogel.

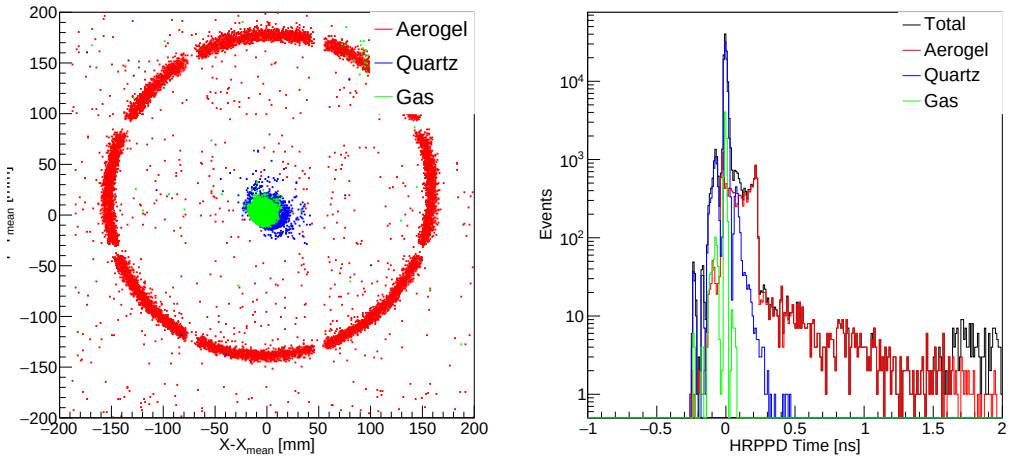

Figure 7.3: Relative impact point of detected photons on the sensor plane for N_2 gas in expansion volume (left), including aerogel photons (left) and timing of these photons in comparison (right).

Effect of pfRICH material on electron reconstruction in the backward EMCal

The backward acceptance of the EIC detector is crucial for measuring the scattered electron from DIS. It is equipped with a high resolution EMCal based on $PbWO_4$ crystals. Any material in the line-of-sight from the collision vertex to EMCal may distort electron measurements in the EMCal. The main mechanism for energy losses by a high momentum electron in material is through Bremsstrahlung photon radiation, which for thick enough material may initiate an electromagnetic shower, where the initial energy of a high momentum electron transforms into a cascade of low energy electromagnetic particles. As a result, some part of the initial electron energy may be absorbed in the material before reaching the EMCal. From GEANT simulations, such energy losses are predicted to be negligible if the amount of material is below 30% of a radiation length. Another mechanism for the electron energy mis-reconstruction is that the initial electron and radiated photons get separated in the magnetic field and can produce more than one cluster in the EMCal. Some of the lowest energy clusters may get lost below the minimal energy threshold in the EMCal, and some others become mis-associated with the initial electron track. These effects are minimized for the electrons experiencing small field integral $B_{\perp}dl$ (close to the beam line), and/or if the material is located close to the EMCal.

Figure 7.4 shows the distribution of reconstructed energy in the EMCal from an electron cluster. While the energy distribution is nearly gaussian when no material between the interaction point and EMCal is included, a low energy tail appears with the addition of a realistic material budget. This tail comes mainly from the material located close to the collision vertex (beam pipe and service material from the inner tracker). Such an effect decreases with increasing electron energy and becomes negligible at 10 GeV/c. The additional effect from the material associated with the pfRICH is shown to be small, due

to its proximity to the EMCal.

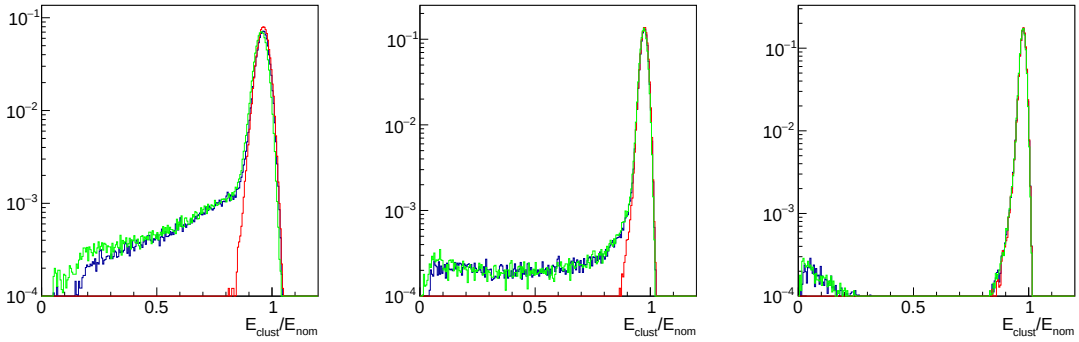

Figure 7.4: Single particle simulation in ePIC detector for $-3.3 < \eta < -1.9$: energy distribution of electron clusters in the backward EMCal for the electron momenta 1 GeV/c (left), 4 GeV/c (middle) and 10 GeV (right); red - with no material effect, blue - with material besides pfRICH, green - with material including pfRICH.